UC Berkeley
UC Berkeley Previously Published Works

Title

A Co(II)-based Molecular Magnet with a 6 T Coercive Field

Permalink

https://escholarship.org/uc/item/7tt0n82b

Authors

Liu, Xiaoqing
Feng, Xiaowen
Zhang, Yuan
et al.

Publication Date

2017-09-22

A Co(II)-based Molecular Magnet with a 6 T Coercive Field

Xiaoqing Liu, [1,2,3†] Xiaowen Feng,[4†] Yuan Zhang,[1†] Liang Li,[5] Xuejing Zhang,[1] Chen Gao,[5] Junliang Liu,[6] Bingwu Wang,[5] Kasper S. Pedersen,[6] Lukas Keller,[7] Yiquan Zhang,[8] Wei Shi,[1,3]* Song Gao,[5] Peng Cheng,[1,2,3]* and Jeffrey R. Long[4]*

[1]College of Chemistry, Key Laboratory of Advanced Energy Materials Chemistry (MOE), Nankai University, Tianjin 300071, China

[2]State Key Laboratory of Elemento-Organic Chemistry, Nankai University, Tianjin 300071, China

[3]Collaborative Innovation Center of Chemical Science and Engineering (Tianjin), Nankai University, Tianjin 300071, China

[4]Department of Chemistry, University of California, Berkeley Berkeley, CA 94720, USA

[5]Beijing National Laboratory of Molecular Science, State Key Laboratory of Rare Earth Materials Chemistry and Applications; College of Chemistry and Molecular Engineering, Peking University, Beijing 100871, China

[6]CNRS, CRPP, UPR 8641, F-33600 Pessac, France

[7]Laboratory for Developments and Methods, Paul Scherrer Institute, CH-5232 Villigen PSI, Switzerland

[8]Jiangsu Key Laboratory for NSLSCS, School of Physical Science and Technology, Nanjing Normal University, Nanjing 210023, China

Hard magnets with high coercivity, such as $Nd_2Fe_{14}B$ and $SmCo_5$ alloys, can maintain magnetisation under a high reverse external magnetic field and have therefore become irreplaceable parts in many practical applications. However, owing to an inherent disadvantage of their preparation process, the magnetic hardness of these intermetallic materials is severely influenced by defects and grain boundaries.[1,2] In this aspect, molecular magnets are promising alternatives, owing to their precise and designable chemical structures, tuneable functionalities and controllable synthetic methods. Here, we demonstrate that an unusually large coercive field of 6 T can be achieved in the antiferromagnetic phase of a single-chain magnet with formula $[Co(hfac)_2(MeONapNIT)]_n$ (MeONapNIT = 2-(2'-(methoxy)naphthyl)-4,4,5,5-tetramethylimidazoline-1-oxyl-3-oxide). Systematic characterisations, including magnetic susceptibility, heat capacity and neutron diffraction measurements, show that the observed giant coercive field originates from the spin dynamics along the one-dimensional chain of the compound because of the strong exchange coupling between Co(II) centres and radicals, and not from three-dimensional magnetic ordering, as is the case for conventional hard magnets.

Magnetism has fascinated human society ever since the discovery of magnetic stones from the island of Magnesia by ancient Greeks. For example, it is known that magnetic materials have been used as compasses for navigation since the 12th century. In the beginning of the 20th century, along with the establishment of the theory of magnetism, magnetic materials found much wider applications in mechanical devices after the industrial revolution, such as in wind-turbines, electric motors and hard drives. Among all the interesting physical properties of a magnetic material, the magnetic hysteresis loop is the key characteristic for practical applications, as it describes how strongly the material can retain its magnetised state.[1] The magnetisation of a magnet can be cancelled by applying an opposing magnetic field. The larger the field required to cancel the magnetisation, also known as the coercive field H_c, the harder the magnet is said to be. A high H_c is required for many technical applications, such as high-density magnetic memories, to avoid information loss due to environmental perturbations. To date, most of the hard magnetic materials are based on intermetallic compounds, such as $Nd_2Fe_{14}B$ and $SmCo_5$ alloys. However, owing to the inherent disadvantage of their preparation process, the magnetic hardness of these intermetallic materials is severely influenced by defects and grain boundaries.[1,2] Thus, a new system that can provide strong and consistent coercivity would be desirable.

Over the past two decades, a number of molecules and one-dimensional chain compounds, known as single-molecule magnets (SMMs)[3,4,5,6,7,8] and single-chain magnets(SCMs),[9,10,11,12,13,14]

respectively, have been shown to retain their magnetisation upon the removal of an applied field. While the relaxation dynamics of SMMs and SCMs share several key characteristics, one pronounced difference is that SCMs always exhibit magnetic hysteresis, because quantum tunnelling is terminated as the chain correlation length increases. As a result, these chain compounds have received considerable attention, owing to their potential applications, such as in high-density information storage.[9–14]

In a SCM, magnetic hysteresis originates from the magnetic anisotropy of the spin carriers and the interactions between them; this was first demonstrated in 2001 in the one-dimensional radical-bridged compound [Co(hfac)$_2$(NITPhOMe)], which has a coercive field of approximately 0.8 T at 2 K (0.5 T at 3.0 K; 0.3 T at 4.5 K).[15] Later, a record-high coercive field of 5.2 T, much higher than that (4.4 T) of the commercial intermetallic magnet SmCo$_5$, was achieved in a similar chain compound with a slightly modified radical ligand.[12] This development indicated that Glauber dynamics are key for the creation of record-hard magnets.[16,17] and attracted considerable research interest in Co(II)-radical chain systems.

However, fine-tuning the magnetic interaction between Co(II) and radicals in a chain in pursuit of a new record for the hardest magnet remains very challenging.[9,12,17,18,19,20] At present, there are no materials, including alloys and molecules, that show a hysteresis loop with a coercive field approaching 6 T under a direct-current (dc) field, especially with a rectangular shape, which is the theoretically ideal shape for hard magnets.

As a continuation of our work on molecular nanomagnets,[21] here we demonstrate an unusually large rectangular hysteresis loop with a giant coercive field of 6 T in a new Co(II)-radical chain compound with the formula [Co(hfac)$_2$(MeONapNIT)]$_n$ (**1**, where MeONapNIT = 2-(2'-(methoxy)naphthyl)-4,4,5,5-tetramethylimidazoline-1-oxyl-3-oxide). Systematic characterisations, including X-ray structural analysis and magnetic susceptibility, heat capacity and neutron diffraction measurements, indicate that the surprisingly large coercive field of **1** originates from the strong intrachain magnetic coupling between Co(II) centres and radicals. Additionally, the building block molecule of **1**, namely, [Co(hfac)$_2$(MeONapNIT)$_2$] (**1'**), was successfully prepared to investigate the magneto-structural correlations in these Co-radical systems.

Results and discussion

By reacting Co(hfac)$_2$·2H$_2$O with MeONapNIT in different molar ratios, we synthesised the crystalline compounds **1'** and **1** (see Methods, Fig. 1). Single-crystal X-ray diffraction analysis revealed that **1'** and **1** crystallise in the monoclinic *C*2/*c* and orthogonal *P*2$_1$2$_1$2$_1$ space groups, respectively. **1'** is a mononuclear complex that contains a Co(II) centre and two terminal MeONapNIT radicals. Linking of **1'** with additional [Co(hfac)$_2$] obtains polymeric **1**, which is composed of a one-dimensional infinite Co(II)–MeONapNIT chain structure.

The coordination geometries of the monomeric **1'** and polymeric **1** were studied with the

semiquantitative method of polytopal analysis[22] and the continuous symmetry measurement method,[23,24] which suggested that the differences between the coordination environments of **1'** and **1** are very small (Supplementary Scheme 1 and Table 1). In **1**, the shortest intrachain Co···Co distances are 7.512(5) Å, and adjacent chains are linked by C-H···F hydrogen bonds to form a three-dimensional supramolecular network with closest interchain Co···Co distances of 10.487(1) Å. It is noted that the shortest Co-O$_{rad}$ bonds of 2.025(8) and 2.023(8) Å of **1'** and **1**, respectively, are the smallest observed thus far in such Co–radical chain systems. This is because the specific hydrogen bonding around the Co(II) centres, in which C16-H16···F5 and C7-H7c···O7 have H···F distances of 2.802(9) and 2.656(6) Å and C-H···F angles of 106.3(4)° and 110.2(9)°, respectively, can further facilitate the coordination between the [Co(hfac)$_2$] moieties and radicals. This short Co-O bond length indicates that strong magnetic coupling between the Co(II) centre and the radical ligand might be present in the compounds (Supplementary Figs. 1 and 2; Supplementary Tables 2 and 3).[9,12,18,20]

To probe the nature of magnetic exchange coupling – firstly in compound **1'** and then in **1** – their static magnetic susceptibilities $\chi_M T$ were measured under a dc field of 0.1 T in the temperature range 2–300 K (Fig. 2a and Supplementary Fig. 3a). The room-temperature $\chi_M T$ of **1'** was 1.40 cm^3 mol^{-1} K, which is much lower than the spin-only value of 2.62 cm^3 mol^{-1} K for one Co(II) ion with two radicals, suggesting very strong intramolecular antiferromagnetic coupling of the monomer **1'**. The fast decrease of temperature–dependence of the $\chi_M T$ of **1'** also showed antiferromagnetic behaviour (Supplementary Fig. 3a). The Hamiltonian employed for the analysis of $\chi_M T$ was $\hat{H} = \mu_B \Sigma g \cdot B \cdot \hat{S}_i - 2J\hat{S}_{radical} \cdot \hat{S}_{Co}$, where J represents the exchange-coupling constant between the Co(II) centre and the radical. The coupling between the radicals was much weaker than J and was not included in the Hamiltonian to avoid overfitting. The dc data were fitted using PHI[25] and the best fit gave $J = -151.7$ cm^{-1}, $g(Co^{II}) = 2.84$ and $zJ' = -10.3$ cm^{-1}, indicating very strong antiferromagnetic coupling between the Co(II) centre and the radical in the monomer.

For the polymer (**1**), the room-temperature $\chi_M T$ was 4.52 cm^3 mol^{-1} K, which is higher than the spin-only value of 2.25 cm^3 mol^{-1} K for one Co(II) ion with one radical owing to the significant orbital contribution from an octahedral high-spin Co(II) ion. Upon lowering the temperature, the $\chi_M T$ product increases to the maximum of 506.44 cm^3 mol^{-1} K at 55 K and then decreases to 23.20 cm^3 mol^{-1} K at 2 K. Based on the similarity of the coordination environments of the Co(II) centres in **1'** and **1**, strong magnetic coupling should occur along the chain. The data of **1** above 65 K were fitted using the branch chain model[19,26] (see Supplementary Information, Section 1.3) to yield the parameters $J = -167.4$ cm^{-1}, $J_a = 167.7$ cm^{-1}, $D = -48.7$ cm^{-1}, $g_R = 2$ (fixed), $g_{Co} = 3.1$ and $k = 0.7$ (fixed) (Supplementary Fig. 4).

For an anisotropic Heisenberg or Ising-like chain system, the $\chi_M T$ product, which is proportional to the correlation length ξ, increases exponentially with decreasing temperature, following the equation $\chi_M T = C_{eff} \exp(\Delta_\xi / k_B T)$, where C_{eff} is effective Curie constant and Δ_ξ is the

correlation energy needed to create a domain wall inside the chain. According to this relationship, the plot of $\ln(\chi_M T)$ vs. $1/T$ should feature a linear region with a slope corresponding to the correlation energy. Thus, to prove the one-dimensional nature of compound **1**, variable-temperature alternating-current (ac) susceptibility data were collected in the absence of a dc field, with an ac field of 3 Oe oscillating at 1 Hz. The resulting plot of $\ln(\chi_M' T)$ vs. $1/T$ (Supplementary Fig. 5) features a linear region. The best fit to the data confirmed the one-dimensional magnetic nature of **1**, with a high correlation energy Δ_ξ/k_B of 387 K (269 cm^{-1}) and a C_{eff} of 1.65 cm^3 mol^{-1} K.

The field dependence of the magnetisation of **1** was studied at different temperatures (Supplementary Fig. 6). At 2 K, the magnetisation of **1** in a magnetic field of 0–4 T was nearly zero, owing to interchain antiferromagnetic coupling. Above 4 T, the magnetisation increased, but it could not be saturated by a 7 T external field. When the external field increased to 14 T, the magnetisation reached the saturation value of 2.1 $N\beta$. Increasing the temperature from 2 to 7 K resulted in similar hysteresis of the magnetisation. When the temperature was higher than 9 K, the magnetisation could be saturated by a 7 T magnetic field.

The magnetisation hysteresis loops were recorded between ±7 or ±14 T in the temperature range 2–14 K at a field-sweeping rate of 100 Oe/s (Fig. 2b and Supplementary Fig. 7). In the temperature range 2–7 K, the hysteresis loops of **1** exhibited a giant coercive field of 6 T.

To the best of our knowledge, 6 T is a record-high value for the coercive field achieved by a dc magnetic field in any type of magnet[6,12,18,20,27,28,29] Moreover, these hysteresis loops are extremely rectangular, with a squareness (M_r/M_s, where M_r is the remanent magnetisation and M_s is the saturation magnetisation) of 97% at 2 K, indicating that **1** can be regarded as the hardest magnet known to date (Supplementary Table 4). This magnet is unique and of high value for both theoretical studies and potential applications if we can understand the magneto-structural correlation.

Increasing the temperature from 8 to 14 K led to the gradual decrease of the coercive fields, and the hysteresis loop closed for temperatures above 14 K. It must be noted that the coercive fields were observed to depend on the field-sweeping rate above 8 K; a higher field-sweeping rate resulted in a broader hysteresis loop[5] (Fig. 2c).

The divergence of the field-cooled (FC) magnetisation and zero-field-cooled (ZFC) magnetisation can show the thermal irreversibility of compound **1** and determine the transition temperature between the paramagnetic and superparamagnetic states.[5] As shown in Supplementary Fig. 8, the divergence temperature of the ZFC/FC curves of **1** increases from 14 K to 40 K when the applied field decreases from 1000 Oe to 50 Oe, which is indicative of low-dimensional magnetism.

To probe the magnetisation dynamics of compounds **1'** and **1**, ac magnetic susceptibility data and dc relaxation data were collected under zero dc field. For **1'**, no magnetisation dynamics

were observed in the ac magnetic susceptibility measurements (Supplementary Fig. 3b). For **1**, both the in-phase and out-of-phase ac signals were strongly frequency- and temperature-dependent (Supplementary Figs. 9–11). However, the peaks of the real parts of the temperature-dependent ac susceptibilities (approximately 46.5 K) did not shift distinctly with changing frequency, indicating the possible presence of magnetic long-range ordering in **1**. By fitting the ac data with the Debye model, as shown in the Cole-Cole plots (Supplementary Figs. 12 and 13), and using the dc relaxations (Supplementary Fig. 14), we obtained the relaxation times at different temperatures. Linear fits by the Arrhenius law of the ac and dc relaxation times of **1** (Supplementary Tables 5–7) resulted in effective energy barriers U_{eff} of 297 cm^{-1} (427 K) and 254 cm^{-1} (366 K) using the pre-exponential factors τ_0 of 4.2×10^{-10} and 1.5×10^{-11} s, respectively (Fig. 2d). The two relaxation processes are mainly induced by the unavoidable antiferromagnetic coupling between neighbouring SCM chains and consequently result in an antiferromagnetic phase.[30] To the best of our knowledge, the energy barrier 297 cm^{-1} (427 K) is the highest value yet observed for an SCM.[31] By using the correlation energy $\Delta_\xi = 269$ cm^{-1} in the expression for the overall relaxation barrier for a chain at the finite-size limit, $\Delta_\tau = \Delta_A + \Delta_\xi$, where Δ_A represents the anisotropy energy and Δ_ξ represents the correlation energy, we obtained a value of $\Delta_A = 28$ cm^{-1}. As this anisotropy energy is almost one order of magnitude lower than the correlation energy (269 cm^{-1}) of compound **1**, the slow magnetic relaxation dynamics of **1** is dominated by the one-dimensional correlation because of the strong intrachain magnetic coupling in chain compound **1**.

To study the nature of the possible transition at the divergence temperatures, specific heat measurements were performed for **1** in the temperature range of 2–50 K under 0, 0.1 and 1.0 T dc fields (Fig. 3). No clear anomalies were identified in any of the original curves owing to the significant contribution of the lattice heat capacity, which covers the signal changes of magnetic contributions. However, anomalies can be observed at approximately 46.5 K if we subtract the in-field heat capacity of the zero-field data (Fig. 3, inset).[32] These anomalies indicate the presence of long-range ordering of the chains and a phase transition at 46.5 K, which is consistent with the results of the in-phase susceptibility measurements. A (*T*, *H*) phase diagram can be obtained by plotting the peak values of the temperature- and field-dependent magnetic susceptibilityies, which can further confirm the antiferromagnetic phase of **1**[30] (Supplementary Fig. 15).

To determine the magnetically ordered structure of **1**, powder neutron diffraction data were acquired between 1.5 and 100 K in zero magnetic field (Supplementary Fig. 16). The results showed that all the normalised diffraction peaks were consistent with the simulated peaks from the single-crystal X-ray diffraction data, indicating the high phase purity of the material. Nevertheless, a negative implication of magnetic ordering was observed because the non-deuterium sample could generate a high background neutron diffraction signal, which was sufficiently strong to cover the ordering signal.[33]

To further study the origin of the giant coercive field observed in compound **1**, *ab initio* CASSCF/RASSI/SINGLE_ANISO calculations were performed on compound **1** and two reported compounds with high coercive fields, $[Co(hfac)_2PyrNN]_n$ (PyrNN = 2-(1'-pyrenyl)-4,4,5,5-tetramethylimidazoline-1-oxyl-3-oxide)[19] and $[Co(hfac)_2BPNN]_n$ (BPNN = 2-(4'-butoxyphenyl)-4,4,5,5-tetramethylimidazoline-1-oxyl-3-oxide).[12] The calculated magnetic axes of the Co(II) centres are shown in Supplementary Fig. 17 and Supplementary Table 8. Among the three compounds, compound **1** has the lowest average angle between the magnetic axis of the Co(II) centre and the direction vertical to the 2_1 screw axis, indicating the largest magnetic moment vertical to the 2_1 screw axis of the chain. This result, combined with the high correlation energy obtained from the experimental data, indicate that the chain of compound **1** is the best SCM synthesised to date.

From the crystallographic packing of the chains in these compounds, the symmetry operations of the space groups play an important role in the arrangements of the chains, and hence influence the directions of their magnetic moments, which govern their magnetic properties. The compound $[Co(hfac)_2PyrNN]_n$[19] has only one type of Co(II) chain crystallised in the $P2_1/c$ space group, whose 2_1 screw axis extends along the *b* axis of each cobalt chain. The directions and the spatial arrangements of the chains and the easy axes of the chains are parallel to each other in this compound (Supplementary Fig. 18). Although compound **1** also contains one crystallographically independent Co(II) centre, its chains exhibit two spatial arrangements – namely, the Co^A and Co^B chains. In addition to the 2_1 screw axis along the chain itself, an additional 2_1 screw axis along the *c* axis of compound **1** generates a different arrangement of the chain (Supplementary Fig. 19). Although the Co^A and Co^B chains in compound **1** are antiferromagnetically coupled, the easy axes of the Co^A and Co^B chains form an angle owing to the symmetry requirement of the crystal. Based on these crystal structures, we consider that two magnetic sublattices exist in compound **1** and only one magnetic lattice exists in $[Co(hfac)_2PyrNN]_n$. As shown in Fig. 4, after magnetisation saturation and demagnetisation under zero external field, the magnetic moments of the chains align along their tilted easy axes. Upon further demagnetisation to the coercive field, a higher external field is required to make the magnetic moments deviate from the easy axes and become antiparallel to each other than that required in the case of $[Co(hfac)_2PyrNN]_n$; this is another important aspect for the giant coercive field. Based on this discussion, the full formation of the hysteresis loop is depicted in Fig. 4 and Movie S1. Additionally, a similar case to compound **1** can be found in $[Co(hfac)_2BPNN]_n$,[12] which also has two sublattices but from two crystallographically independent Co(II) centres, which are hence responsible for a giant coercive field.

Conclusion

We describe here $[Co(hfac)_2(MeONapNIT)]_n$, a new molecular magnet with a record-high energy barrier can achieve a giant coercive field of 6 T and with an unprecedentedly large hysteresis loop squareness. Detailed structural and physical characterisations showed that the

observed giant coercive field arises from the magnetisation dynamics of the compound, which are based on the strong exchange coupling between Co(II) centres and radicals along the chain. Additionally, the different directions of the orientations of the magnetic chains in the crystal lattice can significantly contribute to the coercive field. Future efforts will focus on extending this system to other transition-metal ions with large magnetic anisotropy and other radicals with different substituent groups to achieve not only stronger exchange coupling but also a well-designed arrangement of the chains for a higher coercive field. It is our hope that in the future, the concept demonstrated herein could ultimately result in new molecular magnets with a high bulk property that are comparable to classical intermetallic magnets.

Methods

Preparation of MeONapNIT

Dark-purple crystalline MeONapNIT was prepared according to the Ullman procedure[34]. Elemental analysis: calculated (found) for $C_{18}H_{21}N_2O_3$: C, 68.40 (68.18); H, 6.75 (7.02); N, 8.93 (8.67) %. Electron paramagnetic resonance (benzene, room temperature) $g = 2.0078$, $\alpha_N = 7.27$ G (Supplementary Fig. 21). FT-IR (cm^{-1}): 1624 (m), 1594 (m), 1470 (m), 1405 (s), 1364 (vs), 1256 (s), 1217 (m), 1143 (m), 1077 (s), 1014 (m), 854 (m), 823 (s), 771 (s), 697 (m), 525 (s), where vs: very strong, s: strong, m: medium and w: weak peak intensity.

Preparation of 1'

A suspension of Co(hfac)$_2$·2H$_2$O (0.4 mmol, 189 mg) in dry n-hexane (30 mL) was heated to reflux for 2 h; then, a solution of MeONapNIT (0.8 mmol, 250 mg) in dry dichloromethane (10 mL) was added. The resulting solution was left for one week to produce dark block crystals of **1'**. Elemental analysis: calculated (found) for $C_{46}H_{44}CoF_{12}N_2O_{10}$: C, 51.55 (51.18); H, 4.13 (3.80); N, 2.61 (2.96) %. FT-IR (cm^{-1}): 1643 (m), 1503 (w), 1408 (m), 1337 (m), 1243 (s), 1185 (vs), 1126 (vs), 812 (m), 742 (m), 660 (m), 577 (m), 525 (m).

Preparation of 1

A solution of Co(hfac)$_2$·2H$_2$O (0.4 mmol, 189 mg) in dry n-hexane (25 mL) was heated to reflux for 2 h; then, a solution of MeONapNIT (0.4 mmol, 125 mg) in dry dichloromethane (5 mL) was added. The resulting solution was left overnight to produce black needle-like crystals of **1**. Elemental analysis: calculated (found) for $C_{28}H_{23}CoF_{12}N_2O_7$: C, 42.76 (42.40); H, 2.95 (2.75); N, 3.56 (3.76) %. FT-IR (cm^{-1}): 1642 (s), 1480 (m), 1394 (w), 1314 (m), 1260 (vs), 1201 (vs), 1131 (vs), 787 (s), 739 (m), 663 (s), 578 (s), 535 (s).

Characterisations

Magnetic susceptibility measurements were performed using a Quantum Design MPMS VSM SQUID magnetometer and a Quantum Design PPMS. A detailed description of the sample preparation for the magnetic studies is included in the Supplementary Methods. All data were corrected for diamagnetic contributions from the eicosane restraint and the core diamagnetism estimated using Pascal's constants.

Further characterisation, computational and crystallographic details are provided in the Supplementary Methods. Crystallographic data were collected using an Agilent Supernova diffractometer and have been deposited in the Cambridge Structural Database as CCDC 1484802 (**1'**) and 1469453 (**1**).

References

1. Blundell, S. *Magnetism in condensed matter* (Oxford University Press Inc., New York, 2001).

2. Skomski, R. *Simple models of magnetism* (Oxford University Press, Oxford, 2008).

3. Sessoli, R., Gatteschi, D., Caneschi, A. & Novak, M. A. Magnetic bistability in a metal-ion cluster. *Nature* **365**, 141−143 (1993).

4. Gatteschi, D. & Sessoli. R. Quantum tunneling of magnetization and related phenomena in molecular materials. *Angew. Chem. Int. Ed.* **42**, 268−297 (2003).

5. Gattschi, D., Sessoli, R. & Villain, J. *Molecular nanomagnets* (Oxford University Press Inc., New York, 2006).

6. Rinehart, J. D., Fang, M., Evans, W. J. & Long, J.R. Strong exchange and magnetic blocking in N_2^{3-}-radical-bridged lanthanide complexes. *Nat. Chem.* **3**, 538–542 (2011).

7. Blagg, R. J. *et al.* Magnetic relaxation pathways in lanthanide single-molecule magnets. *Nat. Chem.* **5**, 673–678 (2013).

8. Liu, J. *et al.* A stable pentagonal bipyramidal Dy(III) single-ion magnet with a record magnetization reversal barrier over 1000 K. *J. Am. Chem. Soc.* **138**, 5441–5450 (2016).

9. Caneschi, A. *et al.* Cobalt(II)-nitronyl nitroxide chains as molecular magnetic nanowires. *Angew. Chem. Int. Ed.* **40**, 1760–176 (2001).

10. Clérac, R., Miyasaka, H., Yamashita, M. & Coulon, C. Evidence for single-chain magnet behavior in a Mn^{III}-Ni^{II} chain designed with high spin magnetic units: a route to high temperature metastable magnets. *J. Am. Chem. Soc.* **124**, 12837–12844 (2002).

11. Coulon, C., Miyasaka, H. & Clérac, R. Single-chain magnets: Theoretical approach and experimental systems. *Struct. Bonding (Berlin)* **122**, 163–206 (2006).

12. Ishii, N., Okamura, Y., Chiba, S., Nogami, T. & Ishida, T. Giant coercivity in a one-dimensional cobalt-radical coordination magnet. *J. Am. Chem. Soc.* **130**, 24–25 (2008).

13. Feng, X-W., Liu, J-J., Harris, T. D., Hill, S. & Long, J. R. Slow magnetic relaxation induced by a large transverse zero-field splitting in a $Mn^{II}Re^{IV}(CN)_2$ single-chain magnet. *J. Am. Chem. Soc.* **134**, 7521–7529 (2012).

14. Ouellette, W., Prosvirin, A. V., Whitenack, K., Dunbar, K. R. & Zubieta, J. A thermally and hydrolytically stable microporous framework exhibiting single-chain magnetism: Structure and properties of $[Co_2(H_{0.67}bdt)_3]\cdot20H_2O$. *Angew. Chem. Int. Ed.* **48**, 2140–2143 (2009).

15. Glauber, R. J. Time-dependent statistics of the Ising model. *J. Math. Phys.* **4**, 294–307 (1963).

16. Sessoli, R. Record hard magnets: Glauber dynamics are key. *Angew. Chem. Int. Ed.* **47**, 5508–5510 (2008).

17. Fidler, J., Schrefl, T., Hoefinger, S. & Hajduga, M. Recent developments in hard magnetic bulk materials. *J. Phys.: Condens. Matter* **16**, S455–S470 (2004).

18. Okamura, Y., Nogami, T. & Ishida, T. The hardest magnet from a coordination polymer of alternating cobalt(II)-radical heterospins. *Chem. Lett.* **38**, 740–741 (2009).

19. Vaz, M. G. F. *et al.* A cobalt pyrenylnitronylnitroxide single-chain magnet with high coercivity and record blocking temperature. *Chem. Eur. J.* **20**, 5460–5467 (2014).

20. Cassaro, R. A. A. *et al.* A single-chain magnet with a very high blocking temperature and a strong coercive field. *Inorg. Chem.* **54**, 9381−9383 (2015).

21. Liu, K. et al. Constraining the coordination geometries of lanthanide centers and magnetic building blocks in frameworks: a new strategy for molecular nanomagnet. *Chem. Soc. Rev.* **45**, 2423−2439 (2016).

22. Muetterties, E. L. & Guggenberger, L. J. Idealized polytopal forms. Description of real molecules description of real molecules referenced to idealized polygons or polyhedra in geometric reaction path form. *J. Am. Chem. Soc.* **96**, 1748–1756 (1974).

23. Zabrodsky, H., Peleg, S. & Avnir, D. Continuous symmetry measures. *J. Am. Chem. Soc.* **114**, 7843–7851 (1992).

24. Pinsky, M. & Avnir, D. Continuous symmetry measures. 5. The classical polyhedra. *Inorg. Chem.* **37**, 5575–5582 (1998).

25. Chilton, N. F., Anderson, R. P., Turner, L. D., Soncini, A. & Murray, K. S. PHI: A powerful new program for the analysis of anisotropic monomeric and exchange-coupled polynuclear *d*- and *f*-block complexes. *J. Comput. Chem.* **34**, 1164–1175 (2013).

26. Koningsbruggen, P. J. V. *et al.* Magnetism of A Cu^{II} bimetallic chain compounds (A = Fe, Co, Ni): one- and three-dimensional behaviors. *Inorg. Chem.* **29**, 3325–3321 (1990).

27. Rittenberg, D. K. *et al.* Large coercivity and high remanent magnetization organic-based magnets. *Adv. Mater.* **12**, 126–130 (2000).

28. Walther, A. *et al.* Micro-patterning of NdFeB and SmCo magnet films for integration into micro-electro-mechanical-systems. *J. Magn. Magn. Mater.* 321, 590–594 (2009).

29. Okamura, Y., Ishii, N., Nogami, T. & Ishida, T. Hard magnets after freezing of spin dynamics of soft magnets in cobalt(II)-radical chain compounds. *Bull. Chem. Soc. Jpn.* **83**, 716–725 (2010).

30. Coulon, C., Clérac, R., Wernsdorfer, W., Colin, T. & Miyasaka, H. Realization of a magnet using an antiferromagnetic phase of single-chain magnets. *Phys. Rev. Lett.* **102**, 167204 (2009).

31. Dhers, S., Feltham, H. L. C. & Brooker, S. A toolbox of building blocks, linkers and crystallisation methods used to generate single-chain magnets. *Coord. Chem. Rev.* **296**, 24–44 (2015).

32. Gomes, A. M., Novak, M. A., Sessoli, R., Caneschi, A., & Gatteschi, D. Specific heat and magnetic relaxation of the quantum nanomagnet $Mn_{12}Ac$. *Phys. Rev. B* **57**, 5021–5024 (1998).

33. Franz, P. *et al.* Crystalline, mixed-valence manganese analogue of prussian blue: Magnetic, spectroscopic, X-ray and neutron diffraction studies. *J. Am. Chem. Soc.* **126**, 16472–16477 (2004).

34. Ullman, E. F., Osiecki, J. H., Darcy, R. Studies of stable free radicals. X. Nitronyl nitroxide monoradicals and biradicals as possible small molecule spin labels. *J. Am. Chem. Soc.* **94**, 7049–7059 (1972).

Acknowledgements

Author contributions

Additional information

Figure 1 | Syntheses and crystal structures of 1' and 1. Reaction of Co(hfac)$_2$·2H$_2$O (a) with MeONapNIT in different molar ratios to form the mononuclear complex **1'** (b) and one-dimensional assembly **1** (c).
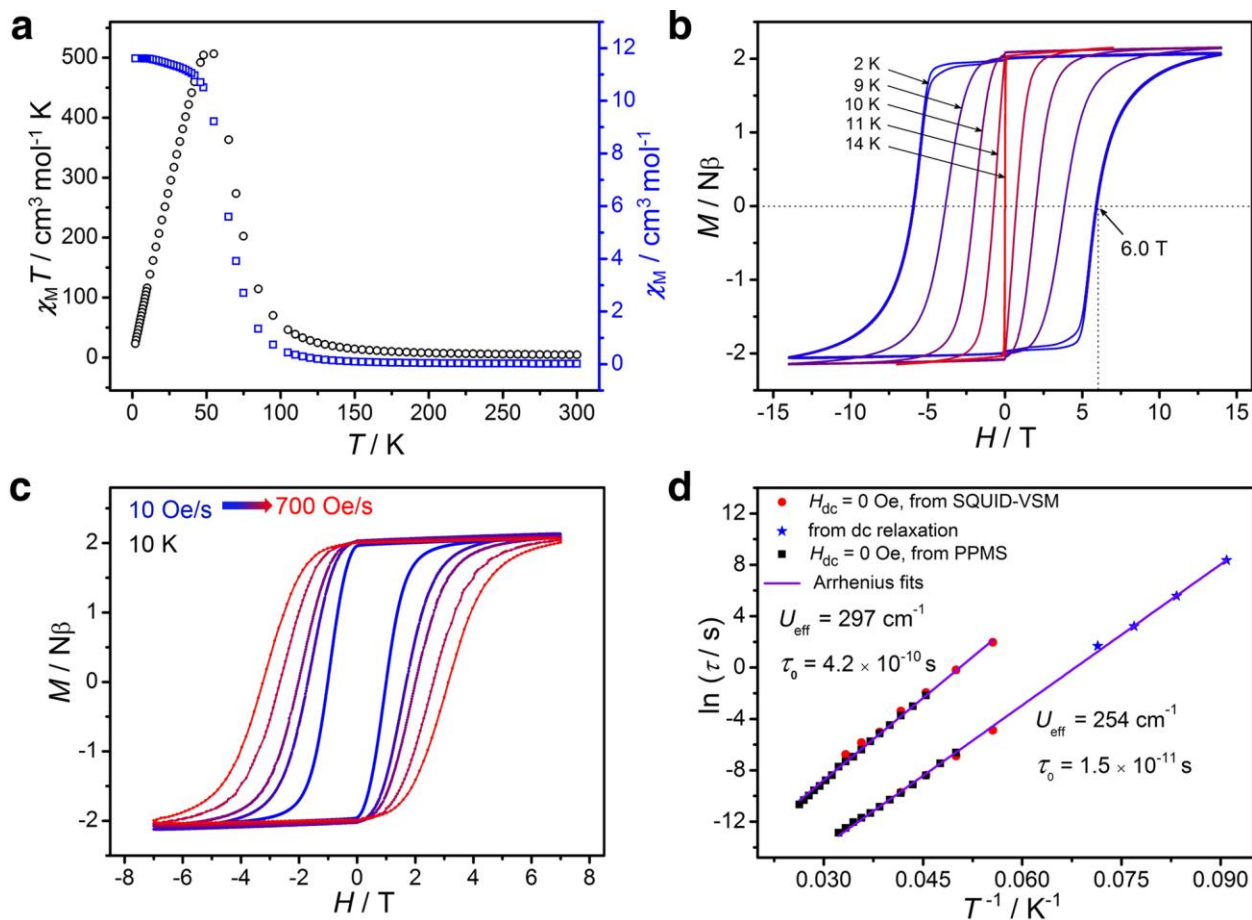
Figure 2 | Magnetic plots of 1. a, Temperature dependence of $\chi_M T$ (black) and χ_M (blue) of **1** measured under a 1000 Oe dc field. **b**, Hysteresis loops of **1** measured at 2, 7, 9, 10, 11 and 14 K with a field sweep rate of 100 Oe/s. **c**, Hysteresis loops of **1** at 10 K with field sweeping rates of 10, 50, 100, 300 and 700 Oe/s. **d**, Plots of $\ln \tau$ *vs.* T^{-1} (τ is the relaxation time) obtained from the ac and dc magnetic susceptibilities of **1**.
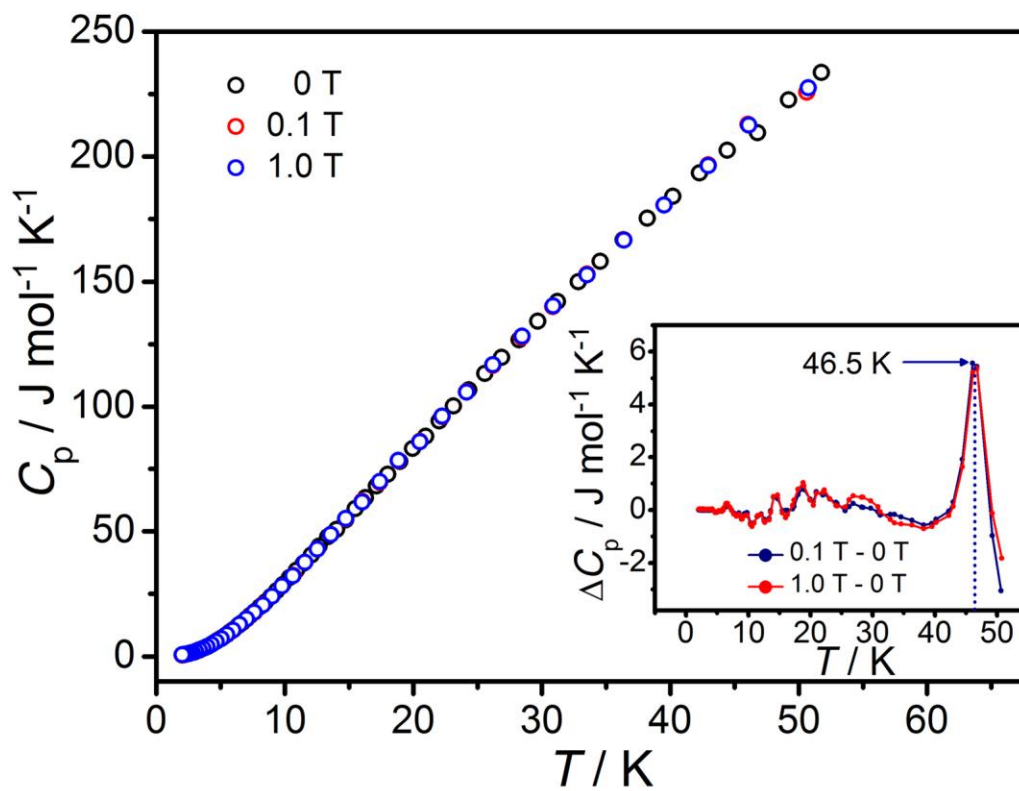
Figure 3 | Specific heat of 1 measured in the temperature range 2–50 K under different applied fields. Inset: subtraction plots of the specific heat capacity.
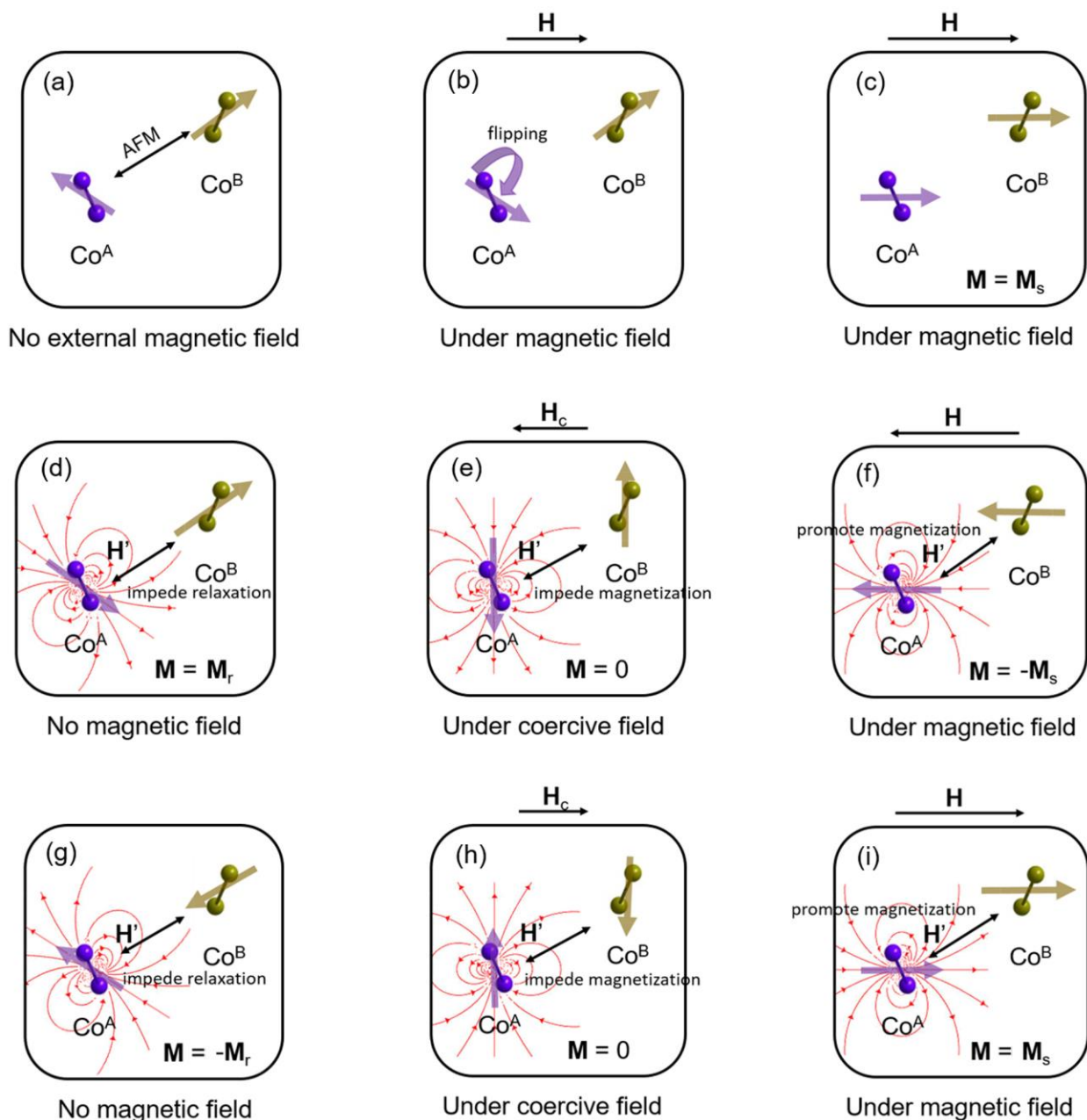
Figure 4 | Magnetisation process of compound 1. Co^A and Co^B represent the magnetic moments of the two sublattices. **a,** No external field. **b,** Under an external magnetic field along the *a* axis, the magnetic moment of the Co^A chain is reversed. **c,** With increasing magnetic field, both chains are magnetised. **d,** An additional field *H'* is applied to each chain, impeding relaxation with decreasing magnetic field. (To simplify the figure, we only show the magnetic field *H'* applied by the Co^A chain.) **e,** *H'* impedes magnetisation before the external field reaches H_c. **f,** After H_c, *H'* promotes the magnetisation of both chains. **g, h, I,** The same processes as those shown in **d**, **e**, **f**, respectively, with the external field reversed.

Supporting information for:

Reaching 6T Mark of Coercive Field in the Antiferromagnetic Phase of a Single-Chain Magnet

Xiaoqing Liu,[1,2,3†] Xiaowen Feng,[4†] Yuan Zhang,[1†] Laing Li,[5] Xuejing Zhang,[1] Chen Gao,[5] Junliang Liu,[6] Bingwu Wang,[5] Kasper S. Pedersen,[6] Lukas Keller,[7] Yiquan Zhang,[8] Wei Shi,[1,3]* Song Gao,[5] Peng Cheng[1,2,3]* and Jeffrey R. Long[4]*

[1]*College of Chemistry, Key Laboratory of Advanced Energy Materials Chemistry (MOE), Nankai University, Tianjin 300071, China*

[2]*State Key Laboratory of Elemento-Organic Chemistry, Nankai University, Tianjin 300071, China*

[3]*Collaborative Innovation Center of Chemical Science and Engineering (Tianjin), Nankai University, Tianjin 300071, China*

[4]*Department of Chemistry, University of California, Berkeley Berkeley, CA 94720, USA*

[5]*Beijing National Laboratory of Molecular Science, State Key Laboratory of Rare Earth Materials Chemistry and Applications; College of Chemistry and Molecular Engineering, Peking University, Beijing 100871, China*

[6]*CNRS, CRPP, UPR 8641, F-33600 Pessac, France*

[7]*Laboratory for Developments and Methods, Paul ScherrerInstitut, CH-5232 Villigen PSI, Switzerland*

[8]*Jiangsu Key Laboratory for NSLSCS, School of Physical Science and Technology, Nanjing Normal University, Nanjing 210023, China*

*Email: shiwei@nankai.edu.cn; pcheng@nankai.edu.cn; jrlong@berkeley.edu

† Those authors contribute equally to this work

Table of Contents

1.0 Materials and General Methods

1.1 Materials

All chemicals and solvents were purchased from commercial sources and used without further purification unless otherwise noted. Dichloromethane, 95.5%, was stirred for at least 6 h over CaH_2 before distillation. Normal hexane and normal heptane, 95%, were dried by distillation over Na.

1.2 Instrumentation

Elemental Analysis (EA) for C, H and N were performed on a Perkin-Elmer 240 CHN elemental analyzer.

Neutron Diffraction measurements were conducted on DMC facilities in Paul Scherrer Institute.

Thermal Gravimetric Analysis (TGA) experiments were carried out on a Netzsch TG-209 instrument with heating rate of 10 °C/min under Nitrogen atmosphere.

Fourier-transform Infrared (FT-IR) spectra (4000-400 cm^{-1}) measurements were implemented on a Bruker ALPHA FT-IR Spectrometer with directly loading powder samples onto the platinum ATR single reflection diamond module. The peak intensities in all spectra are described as very strong (vs), strong (s), medium (m) and weak (w).

Electron Paramagnetic Resonance (EPR) spectra of the organic radicals were recorded on a Bruker EMX-6/1 spectrometer.

X-ray Single Crystal Diffraction data collection were performed on an Agilent Supernova diffractometer at 130 K with graphite-monochromatic Mo Kα radiation (λ = 71.073 pm). The structures were solved by direct methods with SHELXL program and refined by full-matrix least-squares fitting with the SHELXTL software package[1]. CCDC-1484802 and 1469453 contain the supplementary crystallographic data for this paper. The data can be obtained free of charge via www.ccdc.cam.ac.uk.

Crystal data and refinement conditions are presented in Supplementary Table 9.

Selected bonds and angles are listed in the

Static & Dynamic Magnetic Susceptibility measurements were performed on a Quantum Design MPMS VSM SQUID magnetometer and Quantum Design PPMS. All data were corrected for diamagnetic contributions from the eicosane restraint, sample holder, and the compound itself estimated with Pascal's constants. Hysteresis loops collected at 100 K confirmed the absence of ferromagnetic impurities.

Specific Heat measurements were performed on a Quantum Design PPMS small-mass calorimeter employing a semiadiabatic thermal relaxation technique.

1.3 Magnetic properties fitting models

Plot of $\chi_M T$ vs. T of 1 was fitted using uniform branch chain model as described by the following expression 1.

$$\hat{H} = \sum \{ -J[S_{Co,i(z)} \cdot (S_{R,i(z)} + S_{R,i-1(z)})] + J_a L_{Co,i(z)} \cdot S_{Co,i(z)} + D L^2_{Co,i(z)} - \beta H(g_{Co} S_{Co,i(z)} + g_R S_{R,i(z)} + k\, L_{Co,i(z)}) \}$$

Expression 1:

$$\chi T = \frac{N\beta^2}{k_B} \frac{[u^2 a + 2uc + \frac{(ua+c)^2}{b} + d]}{(a+b)}$$

Wherein,

$a = (2e^z \cosh 3y + 1)\cosh 6x + (2e^z \cosh y + 1)\cosh 2x$;

$b = 2[e^z(\cosh 3y + \cosh y) + 1]$;

$c = \{e^z[e^{-3y}(3v - k) + e^{3y}(3v + k)] + 3v\}\sinh 6x + \{e^z[e^{-y}(v - k) + e^y(v+k)] + v\}\sinh 2x$;

$d = \{e^z[e^{-3y}(3v - k)^2 + e^{3y}(3v + k)^2] + (3v)^2\}(1 + \cosh 6x) + \{e^z[e^{-y}(v - k)^2 + e^y(v + k)^2] + v^2\}(1 + \cosh 2x)$;

$u = g_R / 2$;

$v = g_{Co} / 2$;

$x = J / 4k_B T$;

$y = -J_a / 2k_B T$;

$z = -D / k_B T$.

Definitions:

(1) J represents the intrachain exchange;

(2) g_{Co} and g_R correspond to the Landé factors of Co(II) ion and the radical, respectively;

(3) The single-ion anisotropy parameter D was confined to fall in the range of -100 ~ 100 cm^{-1},[2] meanwhile fixing the orbital reduction factor k to 0.7 as typically obtained for six-coordinated Co(II)to avoid over parametrization.

(4) J_a denotes the effective spin-orbit coupling.

Double Relaxations can be described by linear combination of two modified Debye models as described by expression 2.

Expression 2:

$$\chi_{AC}(\omega) = \chi_{S,tot} + \frac{\Delta\chi_1}{1 + (i\omega\tau_1)^{(1-\alpha_1)}} + \frac{\Delta\chi_2}{1 + (i\omega\tau_2)^{(1-\alpha_2)}}$$

Wherein,

$$\Delta\chi_1 = \chi_{T1} - \chi_{S1}$$

$$\Delta\chi_2 = \chi_{T2} - \chi_{S2}$$

$$\chi_{S,tot} = \chi_{S1} + \chi_{S2}$$

The χ_{AC} expression could be split into real and imaginary parts as follows:

$$\chi'(\omega) = \chi_{S,tot} + \Delta\chi_1 \frac{1 + (\omega\tau_1)^{(1-\alpha_1)}\sin(\pi\alpha_1/2)}{1 + (\omega\tau_1)^{(1-\alpha_1)}\sin(\pi\alpha_1/2) + (\omega\tau_1)^{(2-2\alpha_1)}}$$
$$+ \Delta\chi_2 \frac{1 + (\omega\tau_2)^{(1-\alpha_2)}\sin(\pi\alpha_2/2)}{1 + (\omega\tau_2)^{(1-\alpha_2)}\sin(\pi\alpha_2/2) + (\omega\tau_2)^{(2-2\alpha_2)}}$$

$$\chi''(\omega) = \Delta\chi_1 \frac{1 + (\omega\tau_1)^{(1-\alpha_1)}\cos(\pi\alpha_1/2)}{1 + (\omega\tau_1)^{(1-\alpha_1)}\cos(\pi\alpha_1/2) + (\omega\tau_1)^{(2-2\alpha_1)}}$$
$$+ \Delta\chi_2 \frac{1 + (\omega\tau_2)^{(1-\alpha_2)}\cos(\pi\alpha_2/2)}{1 + (\omega\tau_2)^{(1-\alpha_2)}\cos(\pi\alpha_2/2) + (\omega\tau_2)^{(2-2\alpha_2)}}$$

2.0 Synthesis

Preparation of MeONapNIT: Dark Purple crystalline MeONapNIT was prepared according to the Ullman procedure [3]. Elemental analysis: calculated (found) for $C_{18}H_{21}N_2O_3$: C, 68.40 (68.18); H, 6.75 (7.02); N, 8.93 (8.67) %. EPR (benzene, room temp.) $g = 2.0078$, $\alpha_N = 7.27$ G (Supplementary Fig 21). IR (cm^{-1}): 1624 (m), 1594 (m), 1470 (m), 1405 (s), 1364 (vs), 1256 (s), 1217 (m), 1143 (m), 1077 (s), 1014 (m), 854 (m), 823 (s), 771 (s), 697 (m), 525 (s).

Preparation of [Co(hfac)₂(MeONapNIT)₂] **(1')** A suspension of Co(hfac)₂·2H₂O (0.4 mmol, 189 mg) in dry n-hexane (30 mL) was heated to reflux for 2h, then a solution of MeONapNIT (0.8 mmol, 250mg) in dry dichloromethane (10 mL) was added. The resulted solution was left one week to give dark block crystals of **1'**. Elemental analysis: calculated (found) for $C_{46}H_{44}CoF_{12}N_2O_{10}$: C, 51.55 (51.18); H, 4.13 (3.80); N, 2.61 (2.96) %. IR (cm^{-1}): 1643 (m), 1503 (w), 1408 (m), 1337 (m), 1243 (s), 1185 (vs), 1126 (vs), 812 (m), 742 (m), 660 (m), 577 (m), 525 (m).

Preparation of [Co(hfac)₂(MeONapNIT)]ₙ **(1)** A solution of Co(hfac)₂·2H₂O (0.4 mmol, 189 mg) in dry n-hexane (25 mL) was heated to reflux for 2h, and then a solution of MeONapNIT (0.4 mmol, 125mg) in dry dichloromethane (5 mL) was added. The resulted solution was left overnight to give black needlelike crystals of **1**. Elemental analysis: calculated (found) for $C_{28}H_{23}CoF_{12}N_2O_7$: C, 42.76 (42.40); H, 2.95 (2.75); N, 3.56 (3.76) %. IR (cm^{-1}): 1642 (s), 1480 (m), 1394 (w), 1314 (m), 1260 (vs), 1201 (vs), 1131 (vs), 787 (s), 739 (m), 663 (s), 578 (s), 535 (s).

# 3.0 Single Crystal X-ray Crystallography
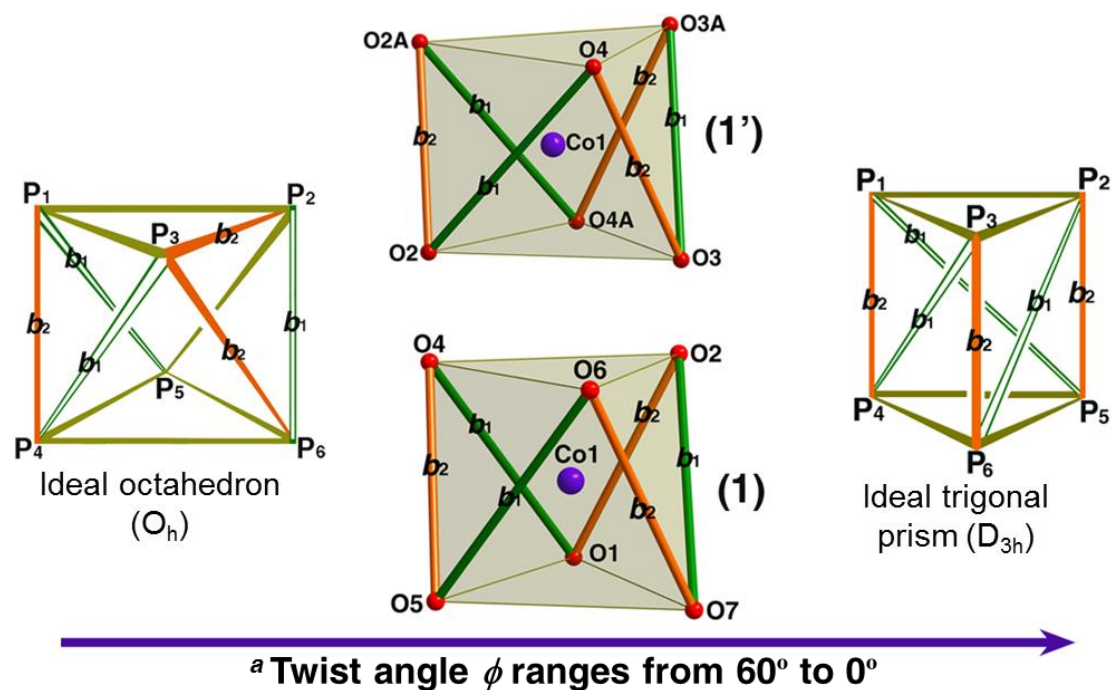
Supplementary Scheme 1. The coordination polyhedra and shape characteristics of Co(II) ions in **1'** and **1** with the twist angles and dihedral angles fall in between those of the ideal octahedron and ideal trigonal prism forms.

[a]The twist angles were calculated by taking the average of the projection angles in the Co-Cen direction, where Cen is the centroid of the top and bottom triangles. The three twist angles were averaged except where a significant spread was observed.
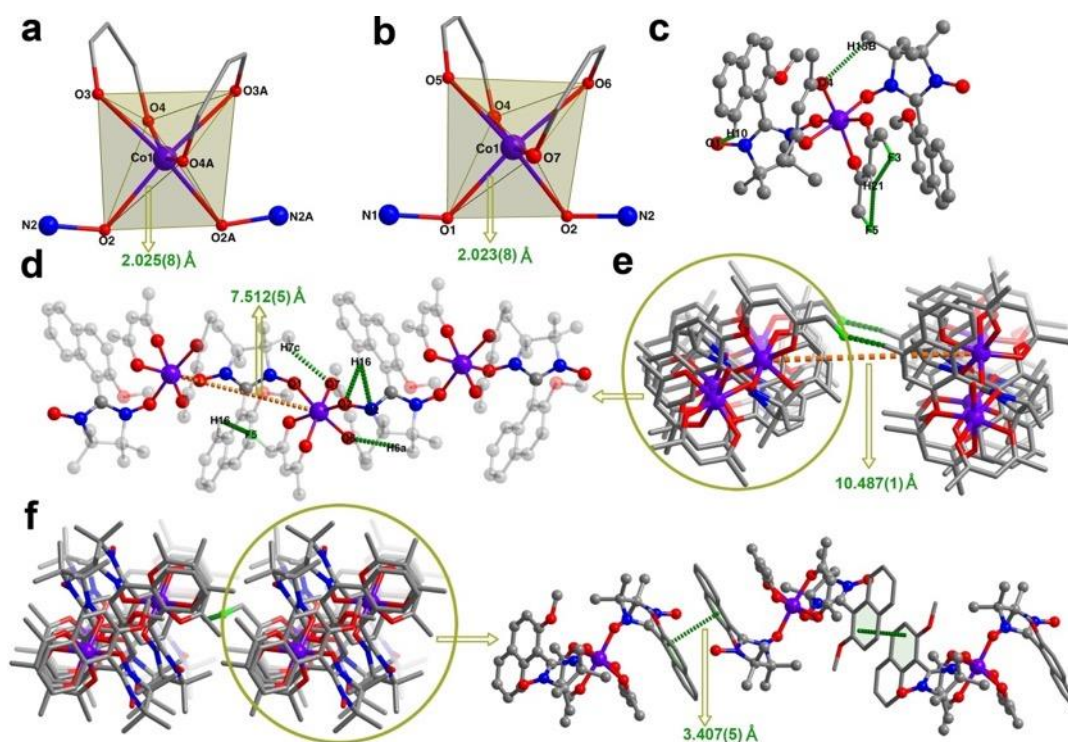
Supplementary Fig. 1 The coordination polyhedra of compounds **1' (a)** (A: –x+1, y, -z+1/2) and **1 (b)**. Intramolecular hydrogen bonds in **1' (c)**. Intrachain hydrogen bonds in **1 (d)**. Packing structures of **1 (e)** and **1' (f)**. Atom color codes: C, gray, N, blue; O, red; Co, purple. All H and F atoms except those forming hydrogen bonds are omitted for clarity.
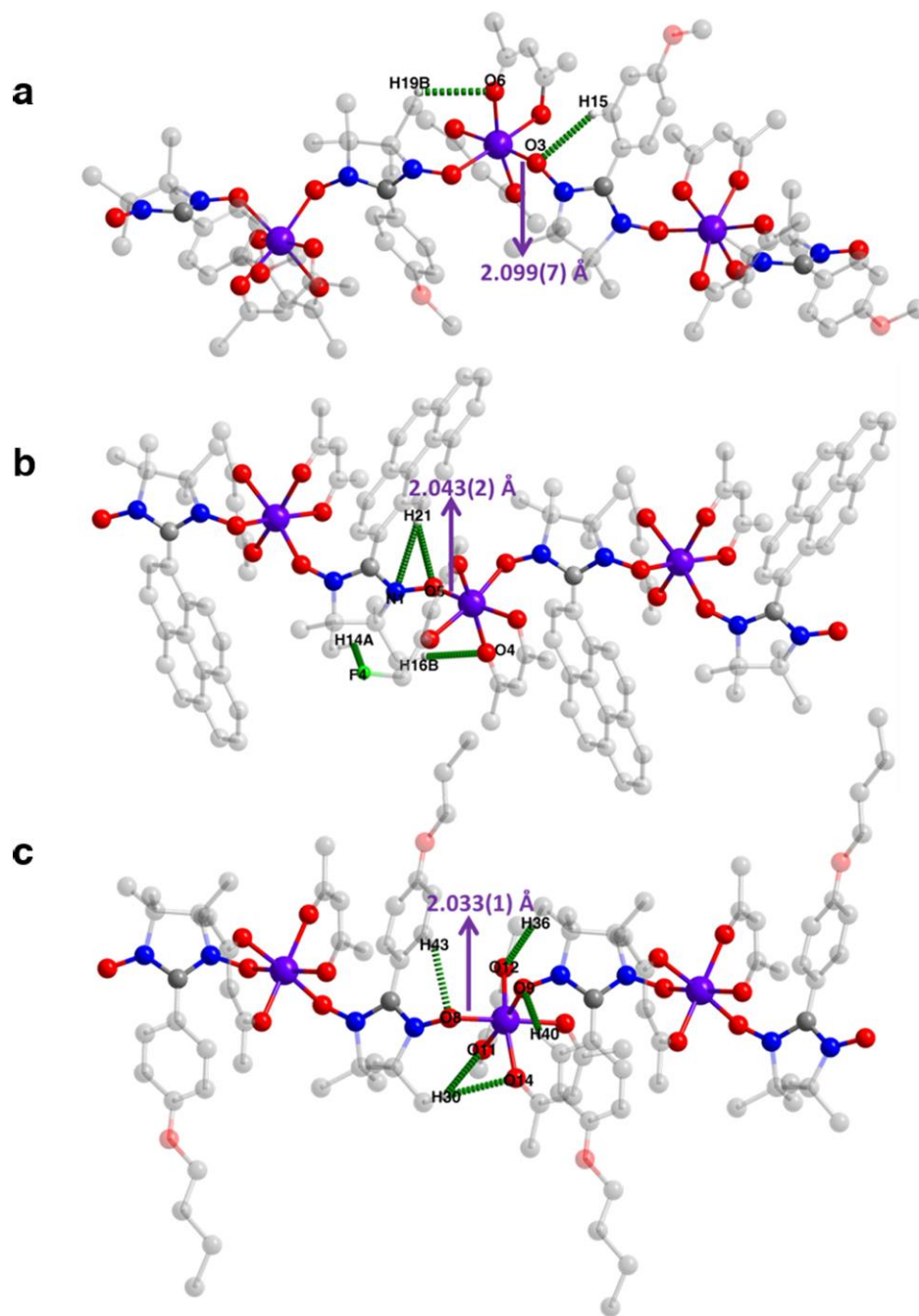
Supplementary Fig. 2 Intrachain hydrogen bonds of $[Co(hfac)_2(NITPhOMe)]_n$[4] **(a)**, $[Co(hfac)_2(PyrNN)]_n$[5] **(b)** and $[Co(hfac)_2(BPNN)]_n$[6] **(c)**. Atom color codes: C, gray, N, blue; O, red; Co, purple. All H and F atoms except those forming hydrogen bonds are omitted for clarity.
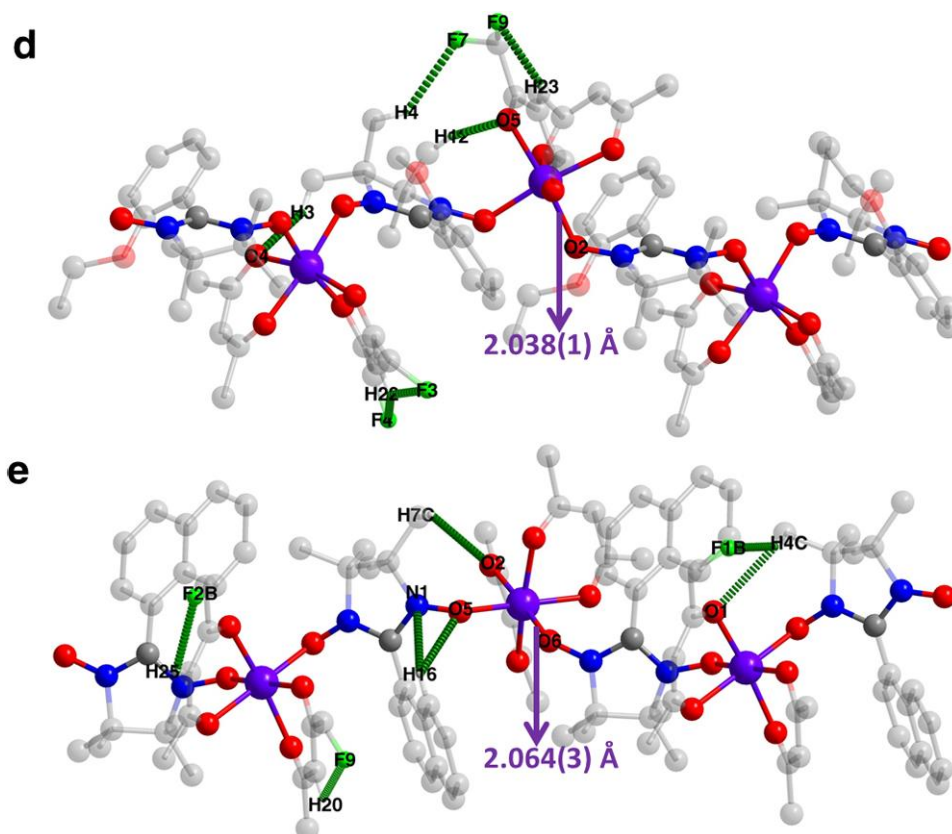
Supplementary Fig. 2 *(continued).* Intrachain hydrogen bonds of [Co(hfac)$_2$(*o*-ethoxyphenylNN)]$_n$[7] **(d)** and [Co(hfac)$_2$(NaphNN)]$_n$[8] **(e)**. Atom color codes: C, gray, N, blue; O, red; Co, purple. All H and F atoms except those forming hydrogen bonds are omitted for clarity.

4.0 Magnetic and Thermal Properties of 1' and 1

4.1 Magnetic properties measurements of 1'
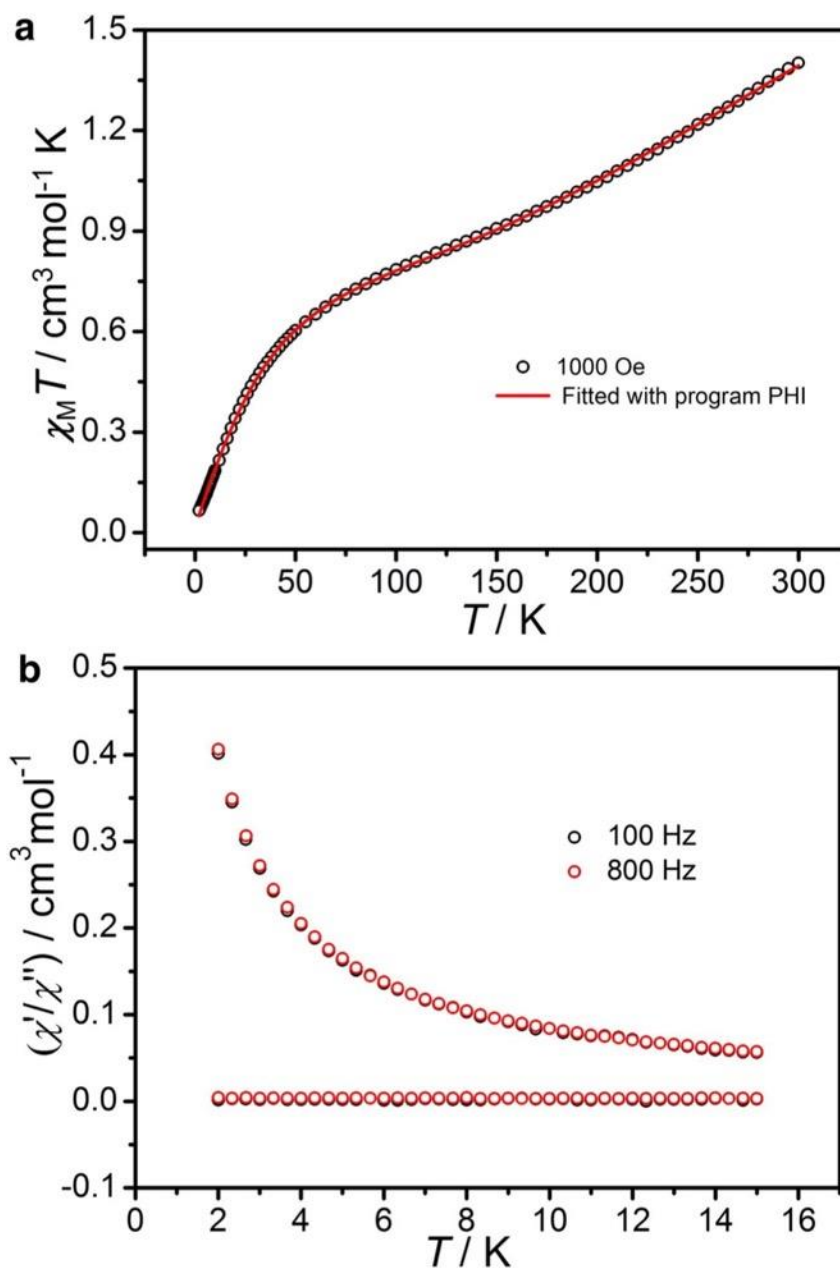
Supplementary Fig. 3 (a) Temperature dependence of $\chi_M T$ for **1'** measured under 1000 Oe dc field. The red line corresponds to the best fit result. **(b)** Temperature dependence of the real χ' and imaginary χ'' components of the ac susceptibilities under zero applied field for **1'**.

4.2 Variable temperature susceptibilities of 1
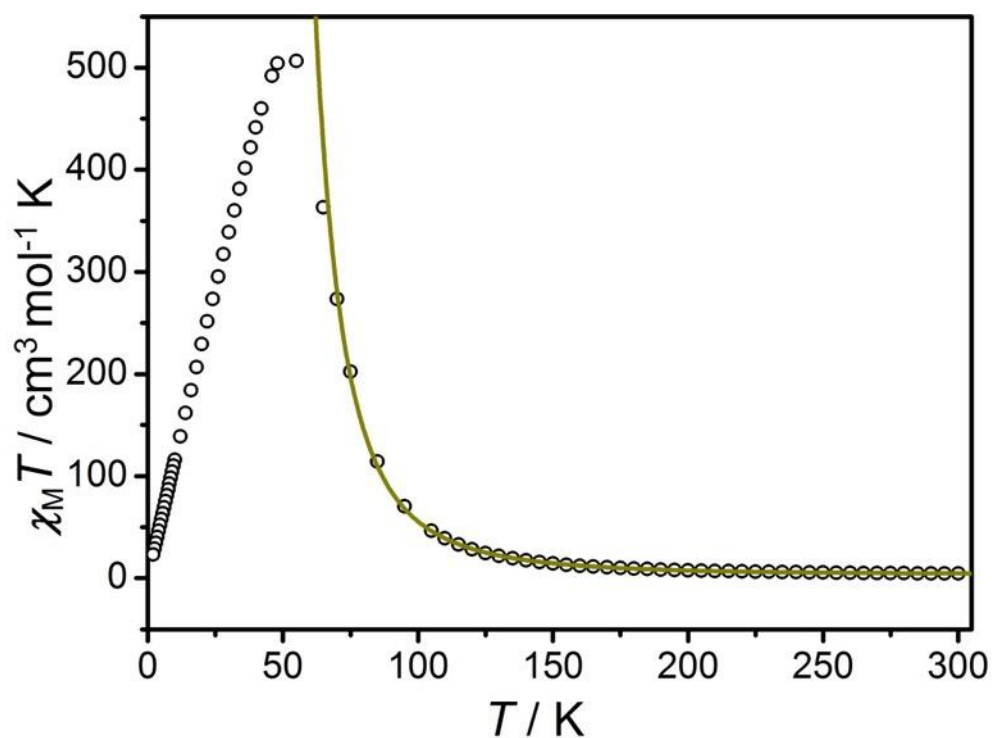
Supplementary Fig. 4 Temperature dependence of $\chi_M T$ of **1** measured under 1000 Oe dc field. The dark-yellow line is a fit to the branch chain model using the data above 65 K yielding the parameter set which best reflects the experimental data: $g_R = 2$, $g_{Co} = 3.1$, $J = -167.4$ cm^{-1}, $J_a = 167.7$ cm^{-1}, $D = -48.7$ cm^{-1} and $k = 0.7$ (fixed).
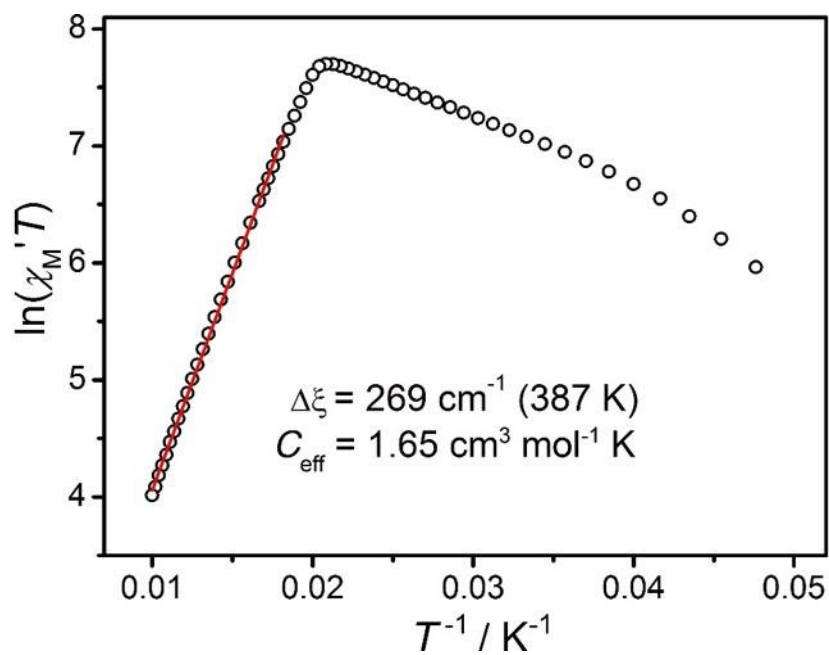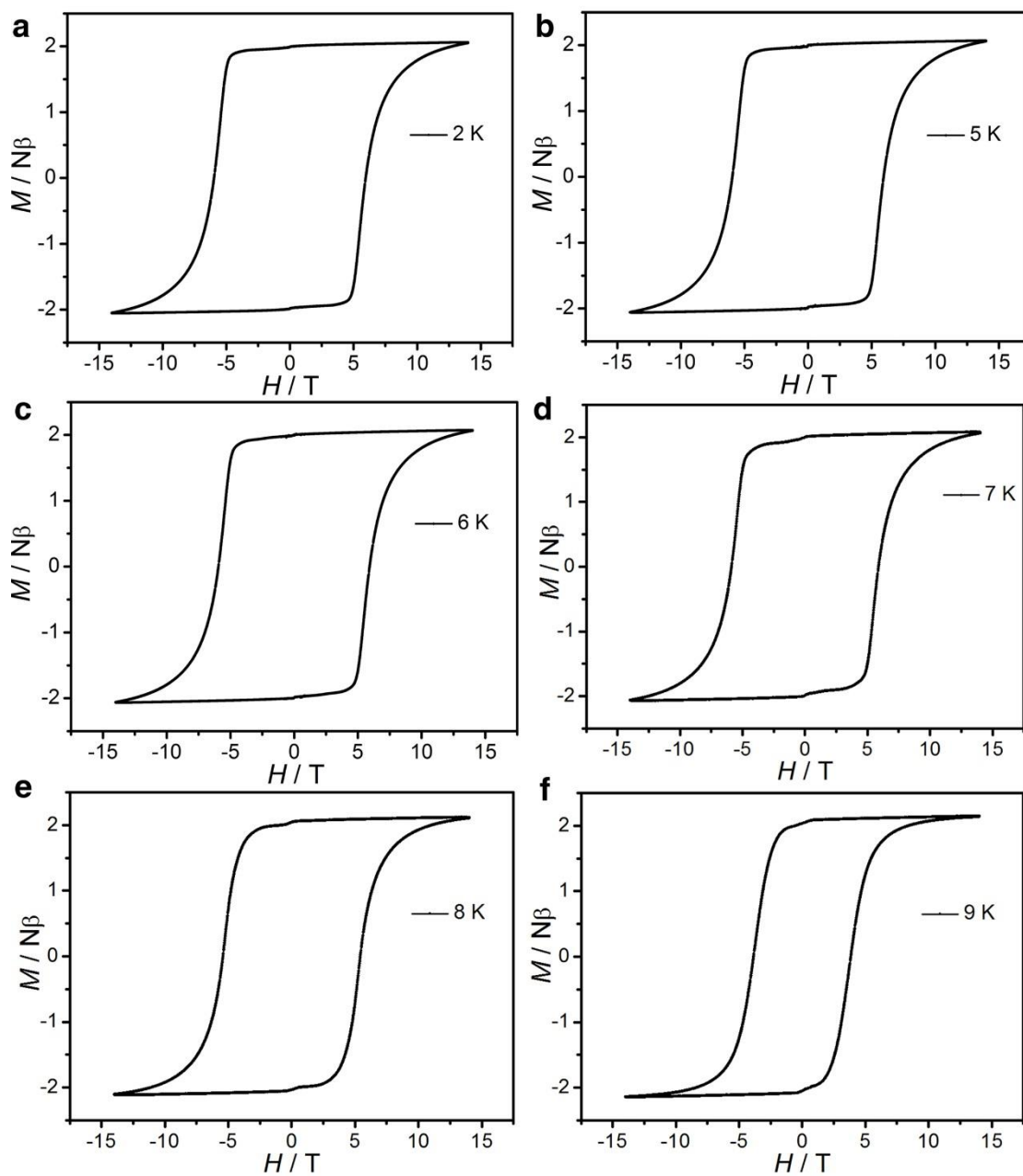
Supplementary Fig. 5 Plot of $\ln(\chi_M'T)$ *vs.* T^{-1} under zero external field for **1**. The solid line corresponds to the linear fitting result.
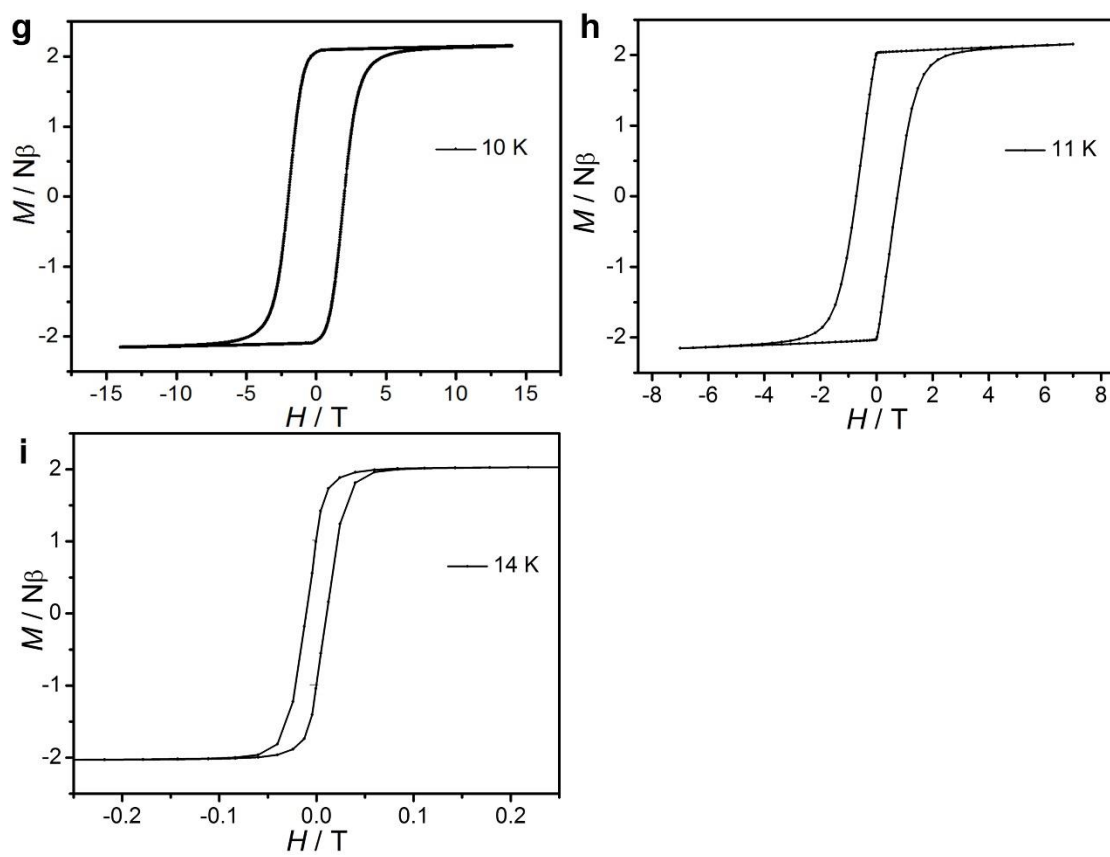
4.3 Variable field magnetizations of 1
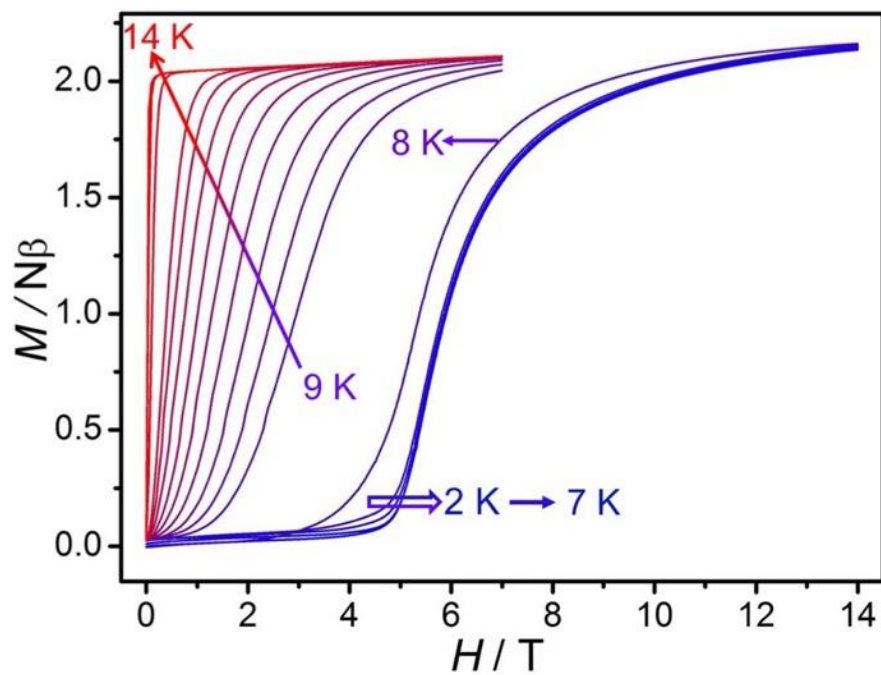
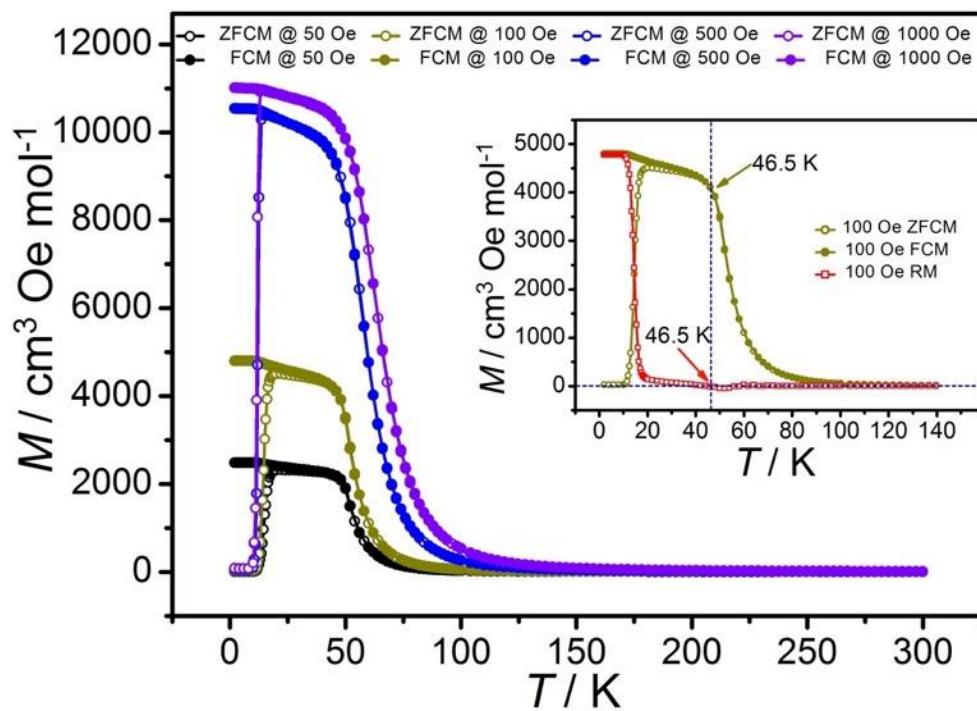**Supplementary Fig. 6** Variable field magnetization (*M*) data of **1** collected from 2 to 14 K.

Supplementary Fig. 7 Hysteresis loops of **1** collected at 2 K **(a)**, 5 K **(b)**, 6 K **(c)**, 7 K **(d)**, 8 K **(e)** and 9 K **(f)** with the field sweep rate of 100 Oe/s.

Supplementary Fig. 7 *(continued)*. Hysteresis loops of **1** collected at 10 K **(g)**, 11 K **(h)** and 14 K **(i)**.

Supplementary Fig. 8 The zero-field-cooled magnetization (ZFCM) and field-cooled magnetization (FCM) at indicated applied fields. Inset: The remnant magnetization (RM) under 100 Oe dc field for **1**.
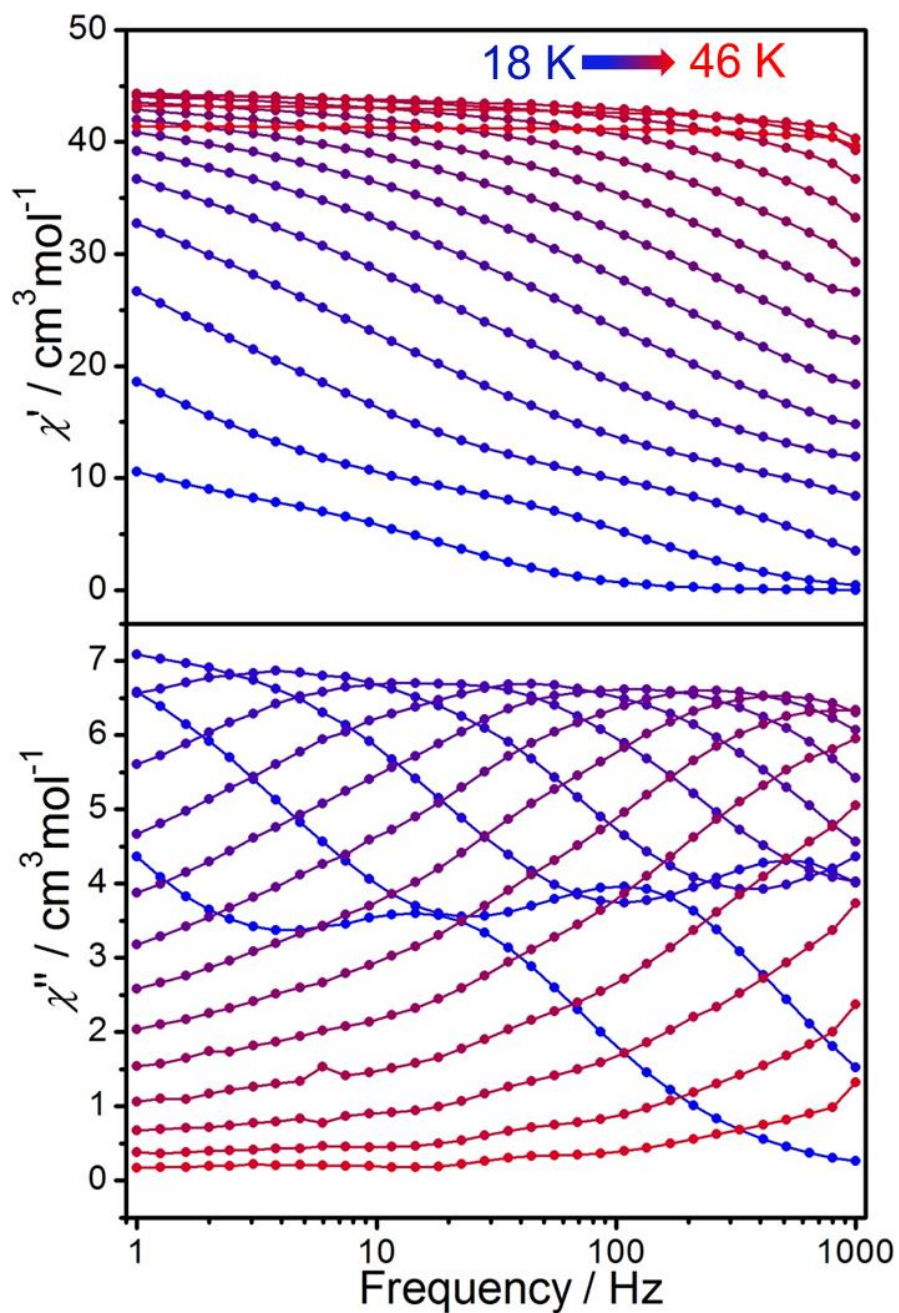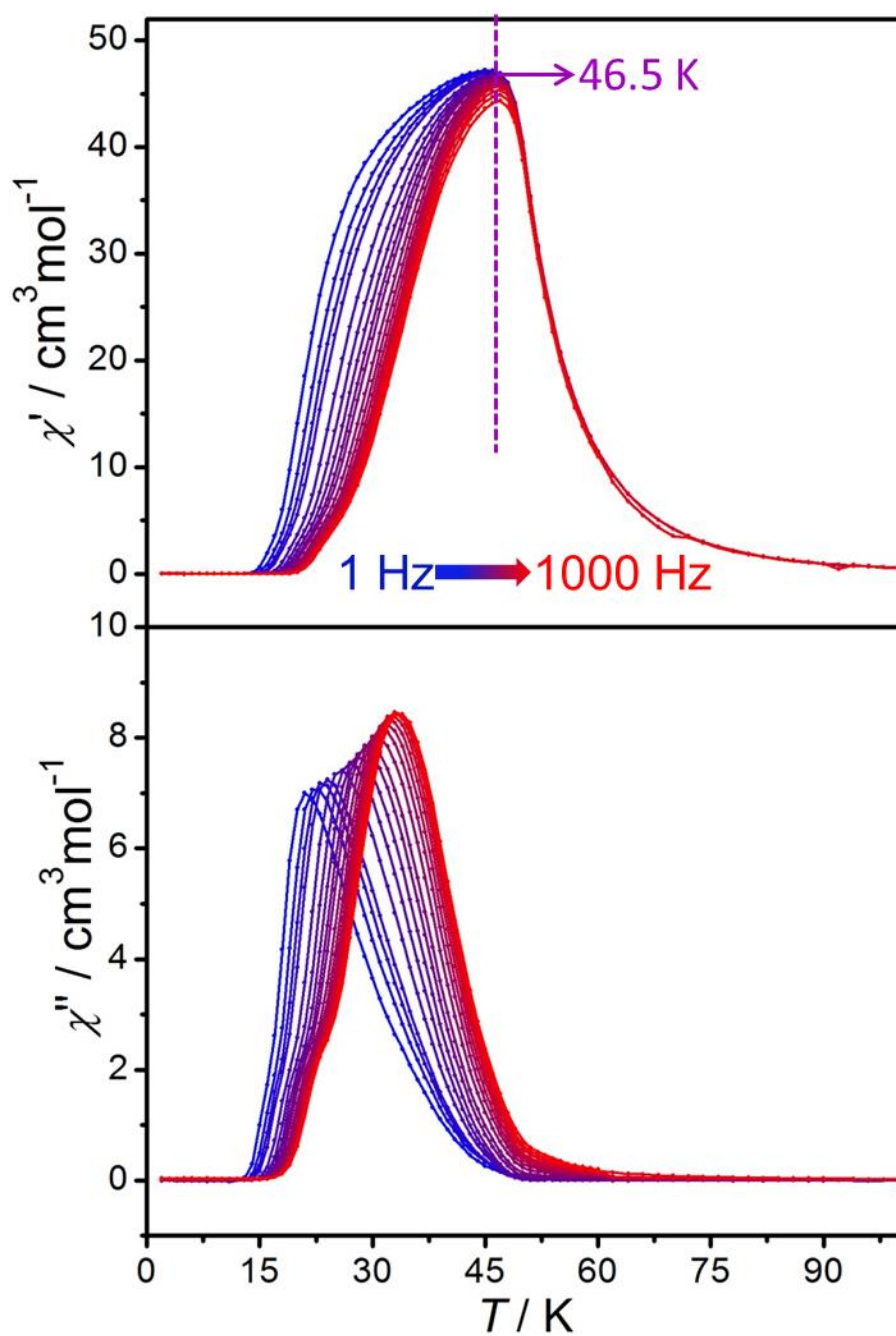
Supplementary Fig. 9 Frequency dependence of in-phase (χ') and out-of-phase (χ'') ac susceptibilities under zero applied field for **1** (1-1000 Hz, by SQUID VSM). The solid lines are guides for the eyes.
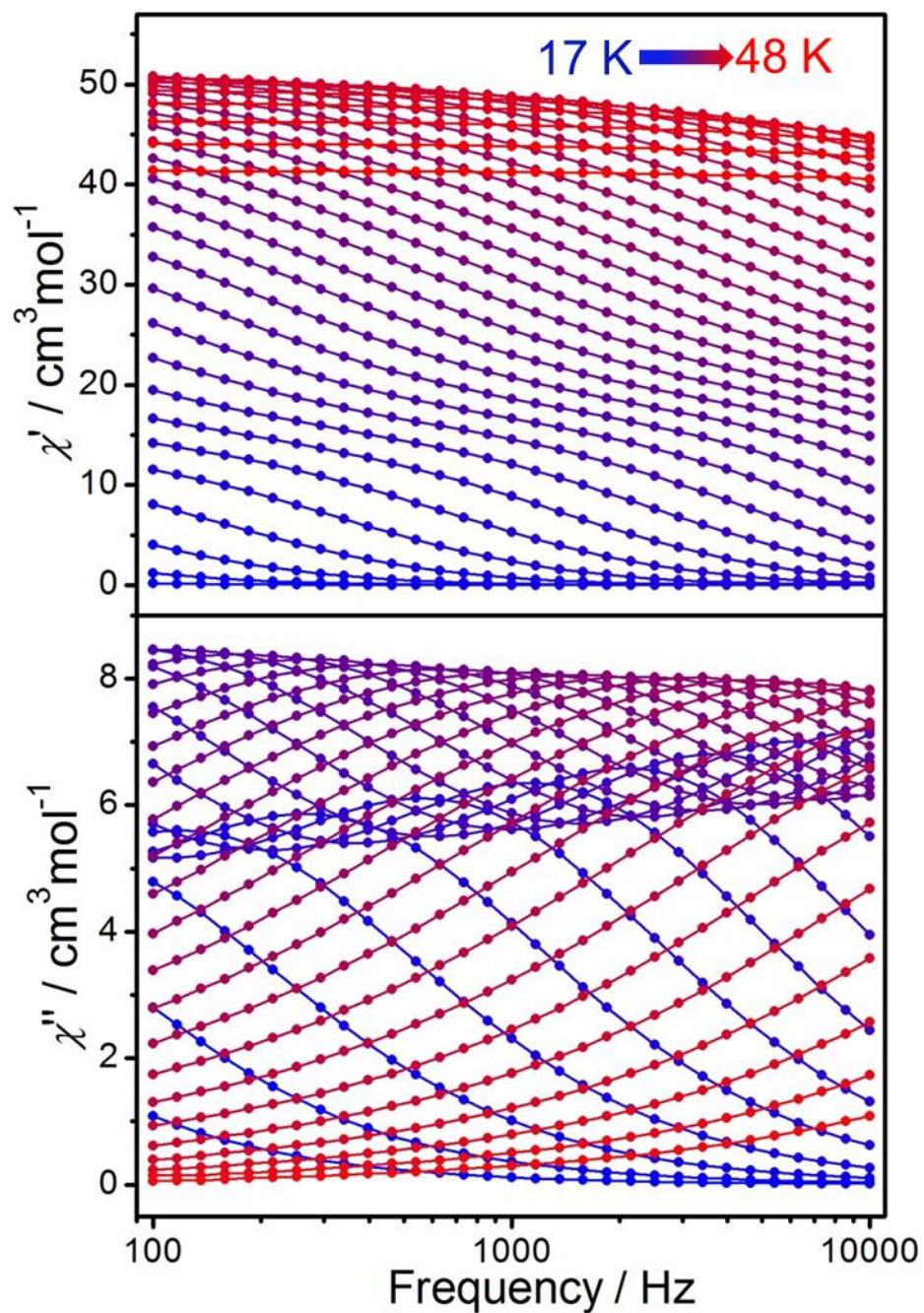
Supplementary Fig. 10 Frequency dependence of in-phase (χ') and out-of-phase (χ'') ac susceptibilities under zero applied field for **1** (100-10000 Hz, by SQUID PPMS). The solid lines are guides for the eyes.

Supplementary Fig. 11 Temperature dependence (by SQUID VSM) of the real and imaginary components of the ac susceptibilities under zero applied field for **1**. The dashed vertical line at 46.5 K indicates the peak temperature of the real part of the ac susceptibilities of **1**.
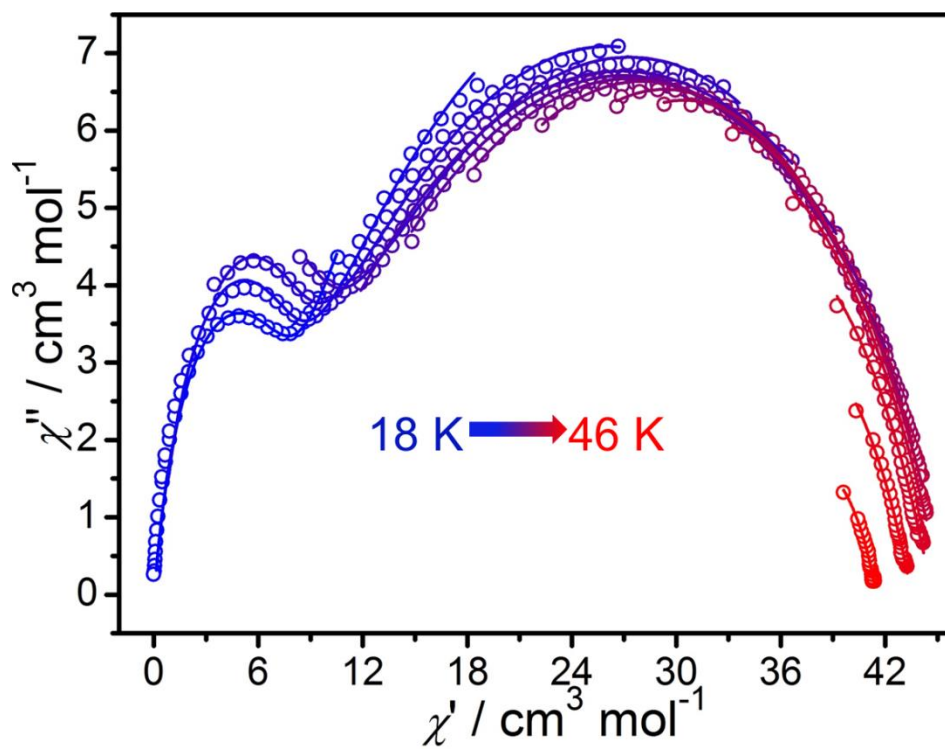
Supplementary Fig. 12 Cole-Cole plots of **1** in the range of 1-1000 Hz by SQUID VSM. The solid lines are fitting results by the general Debye models and linear combination of two modified Debye models at the corresponding temperatures.
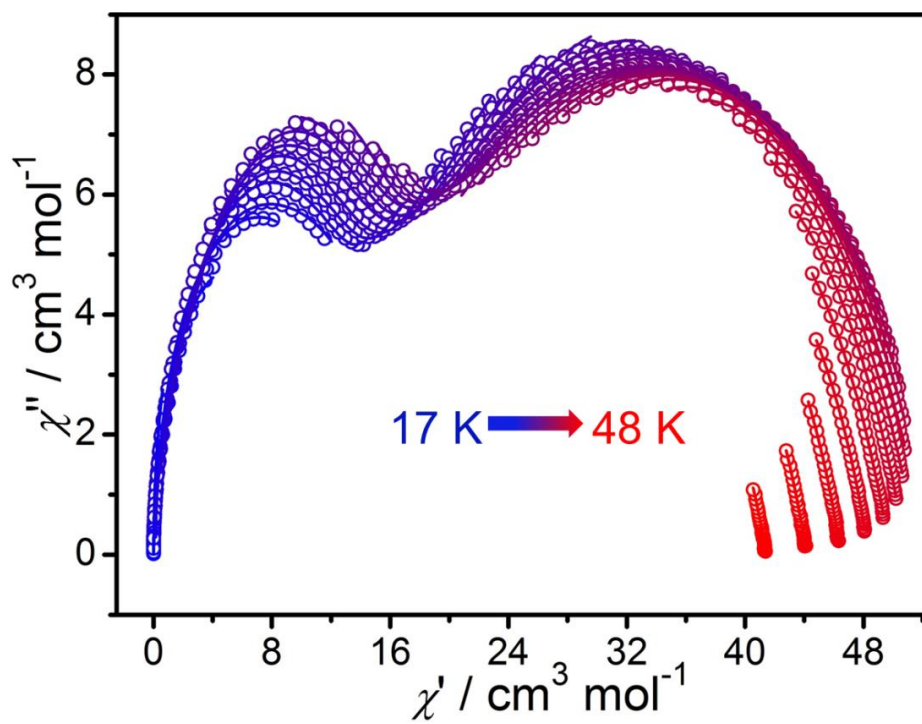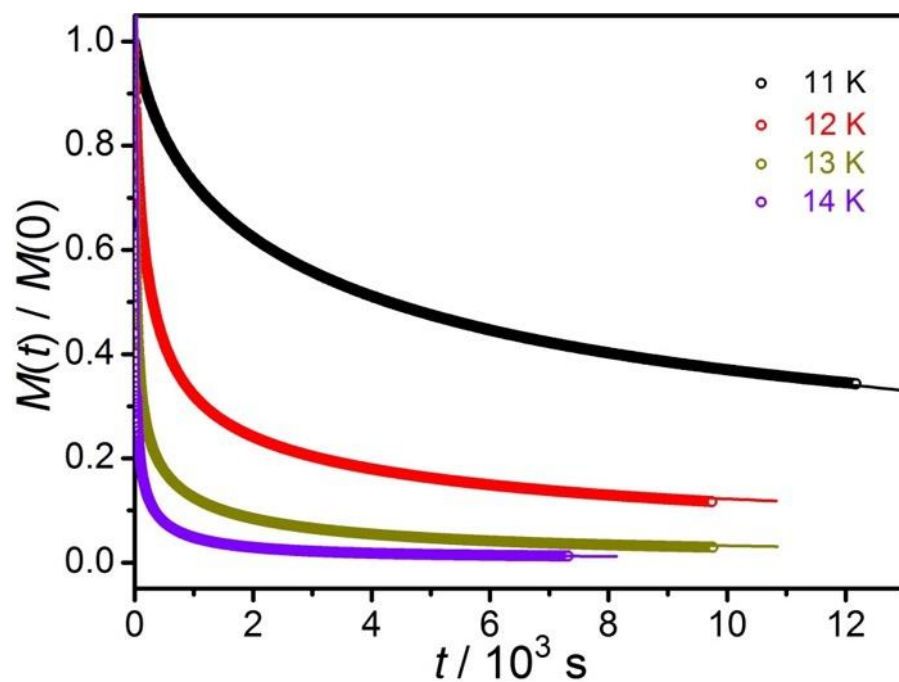
Supplementary Fig. 13 Cole-Cole plots of **1** in the range of 100-10000 Hz by SQUID PPMS. The solid lines are fitting results by the general Debye models and linear combination of two modified Debye models at the corresponding temperatures.

4.6 Dc magnetization relaxation of 1

Supplementary Fig. 14 Plots of normalized magnetization *vs.* time used to deduce relaxation times for **1** at the indicated temperatures by fitting the obtained data to the equation $M_{(t)} = M_f + (M_0 - M_f)\exp[-(t/\tau)^\beta]$ (where τ is the relaxation time). The solid lines correspond to the best fits.

4.7 Magnetic (T, H) phase diagram of 1
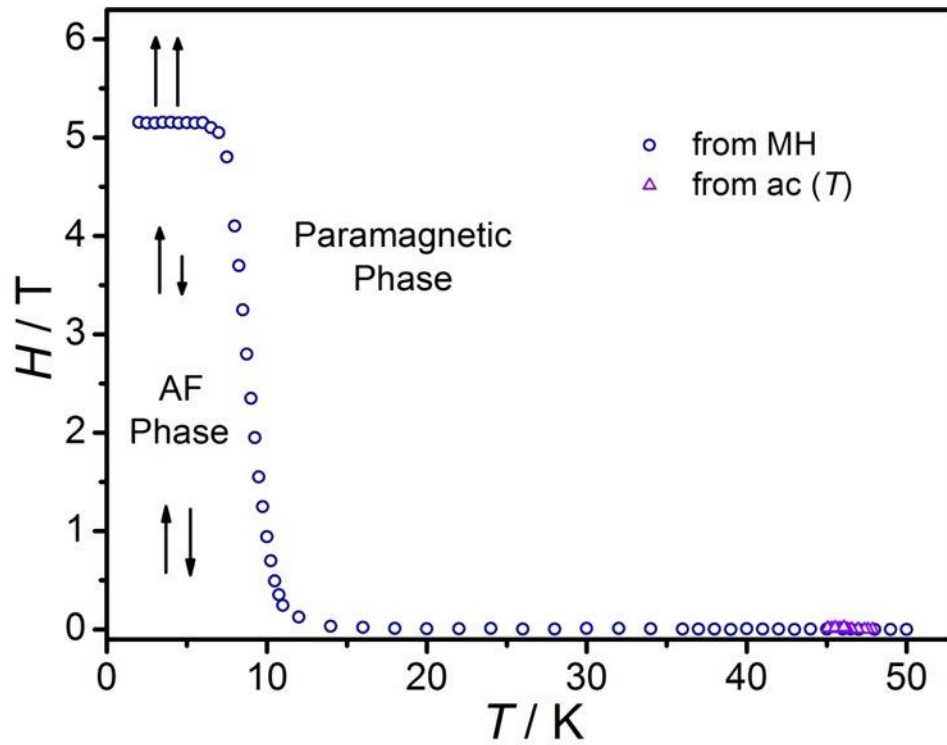
Supplementary Fig. 15 Location of the maximum of susceptibilities from M (*H*) (○) or from the temperature dependence of the ac susceptibilities at a given dc field (△) for **1**. The arrows represent the orientation and magnitude of the two order parameters.

4.8 Neutron powder diffraction of 1
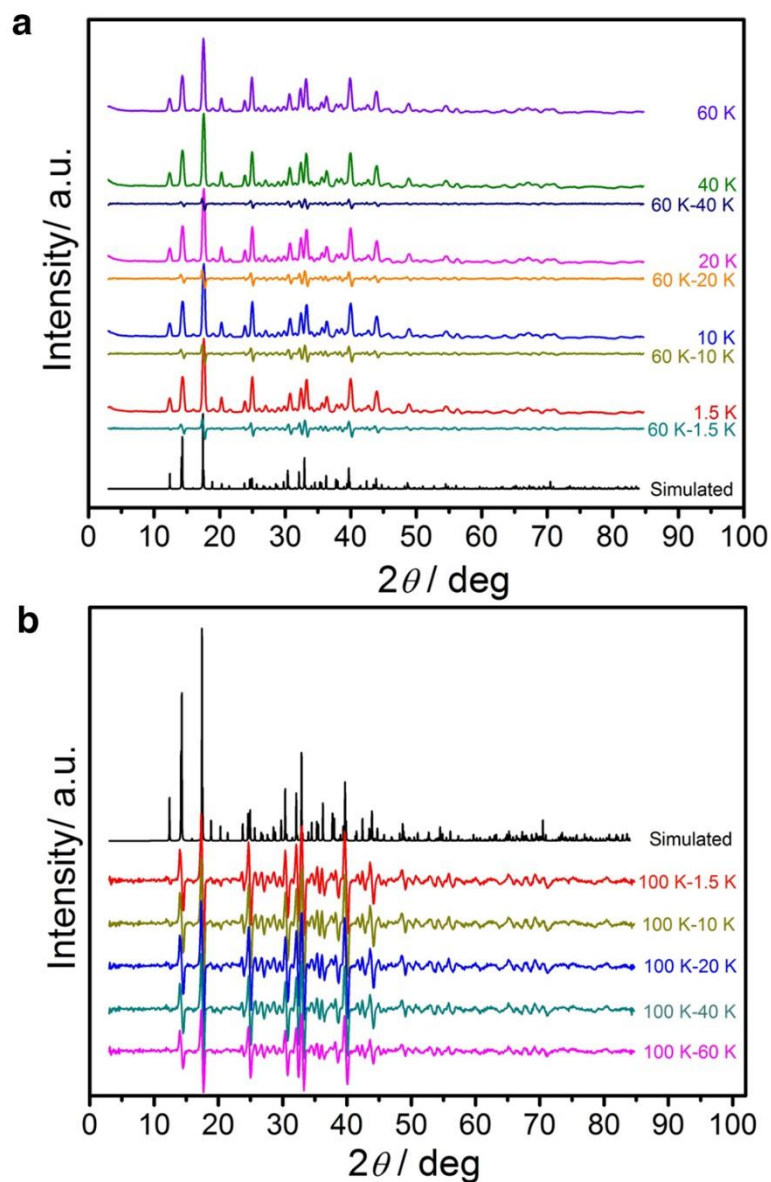
Supplementary Fig. 16 (a) Neutron powder diffraction for **1** at the indicated temperatures and the differences of diffractograms measured at 60 K and 1.5, 10, 20, 40 K, respectively. **(b)** The differences of diffractograms measured at 100 K and 1.5, 10, 20, 40, 60 K, respectively.

5.0 Structural Symmetry Analyses of 1

(a) Compound **1** ($P2_12_12_1$)
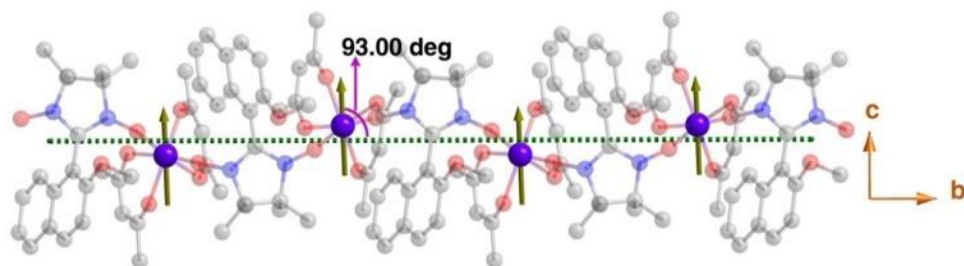
(b) $[Co(hfac)_2(PyrNN)]_n$ ($P2_1/c$)
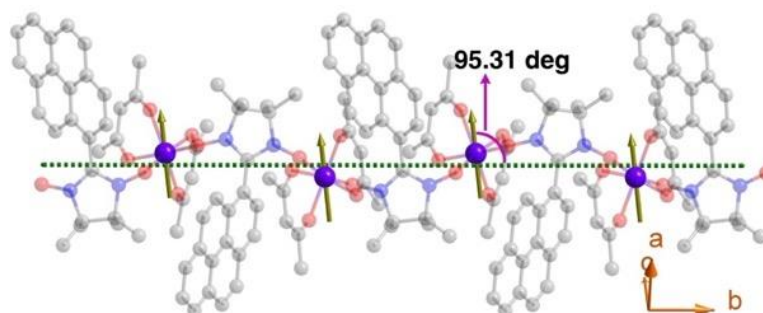
(c) $[Co(hfac)_2(BPNN)]_n$ ($P2_1/n$)
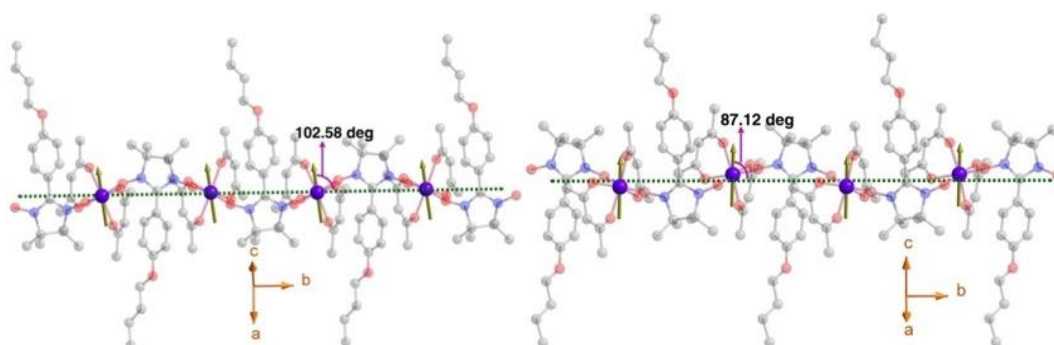
Supplementary Fig. 17 Calculated main anisotropy axes of the metal centers. The dashed lines are 2_1 screw axes of the chains.
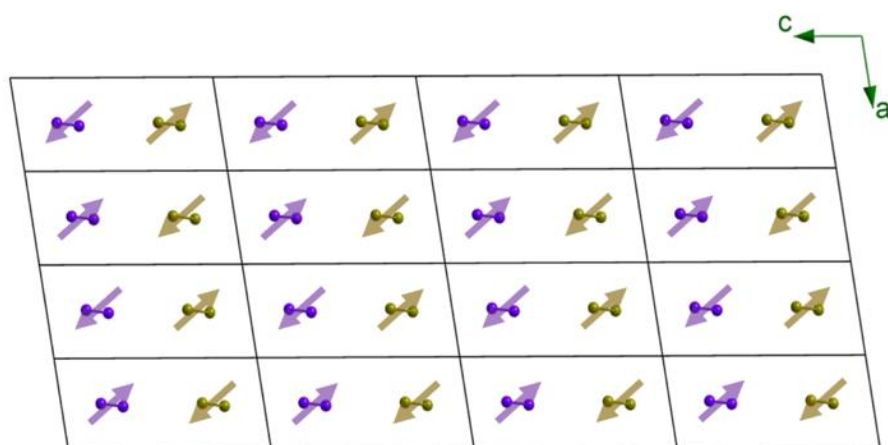
Supplementary Fig. 18 The arrangement of the Co-R chains in [Co(hfac)$_2$(PyrNN)]$_n$[5].

The arrows are the magnetic moments of the chains obtained by *ab initio* calculation.
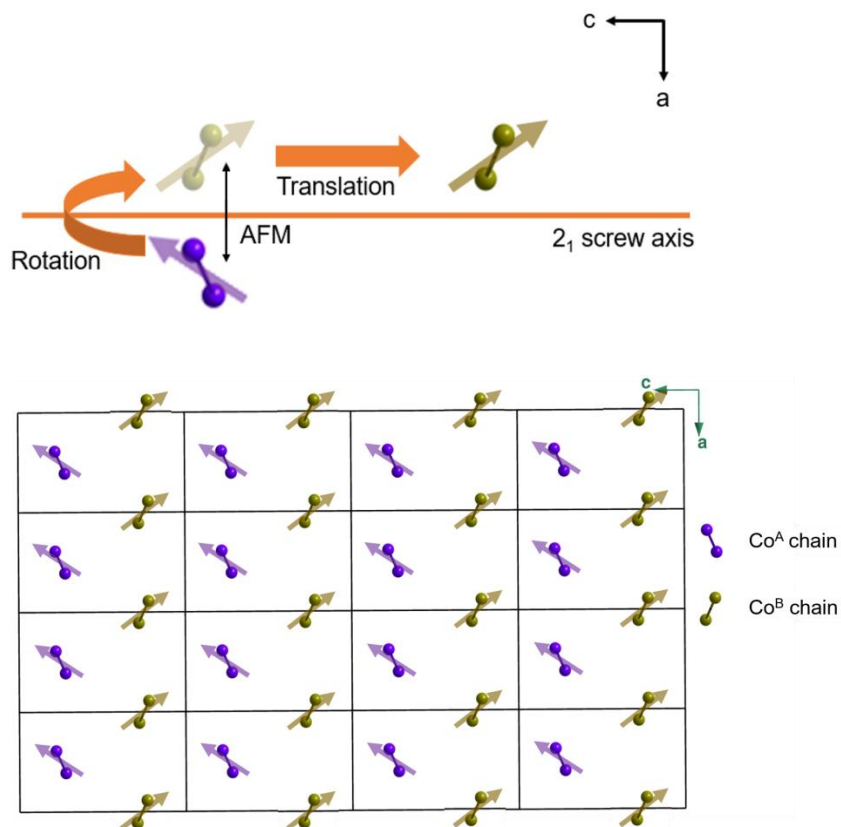
Supplementary Fig. 19 Except the 2_1 screw axis of the chain itself, an additional 2_1 screw axis along c axis generates the second arrangement of the chain (top); the arrangement of the Co-R chains in compound **1** (bottom). The arrows are the magnetic moments of the chains obtained by *ab initio* calculation.

6.0 Tables

Supplementary Table 1. Ideal and observed angles (°) for the six-coordinated compounds **1'** and **1**.

Complex	Semi-quantitative method				Continuous symmetry measure (CSM) method	
	[a] δ's at b_1	δ's at b_2	remaining δ's	[b] ϕ		
Ideal octahedron (O$_h$)	70.5, 70.5, 70.5	70.5, 70.5, 70.5	70.5, 70.5, 70.5, 70.5, 70.5, 70.5	60	O$_h$-OC	D$_{3h}$-TPR
1'	59.977, 55.795, 59.977	86.723, 77.859, 77.859	70.833, 68.040, 76.605, 68.040, 70.833, 76.605	49.0	1.266	10.800
1	59.530, 58.693, 60.334	82.793, 77.038, 78.975	69.062, 72.196, 72.379, 71.783, 70.526, 75.104	47.5	0.925	11.110
Ideal trigonal prism (D$_{3h}$)	0, 0, 0	120, 120, 120	90, 90, 90, 90, 90, 90	0		

[a] δ's at b_1 (b_2) is the dihedral angles, of which b_1 and b_2 denote the reference edges, and [b] ϕ represents the twist angle as demonstrated in the Scheme S1.

Supplementary Table 2. Co-O$_{rad}$ bond lengths [Å] and the O$_{rad}$-Co-O$_{rad}$ angles [°] for compound **1'**, **1**, [Co(hfac)$_2$NITPhOMe]$_n$[4], [Co(hfac)$_2$(PyrNN)]$_n$[5], [Co(hfac)$_2$(BPNN)]$_n$[6], [Co(hfac)$_2$(o-ethoxyphenylNN)]$_n$[7] and [Co(hfac)$_2$(NaphNN)]$_n$[8].

Complex	Compound 1'	Compound 1	[Co(hfac)$_2$ (NITPhOMe)]$_n$	[Co(hfac)$_2$ (PyrNN)]$_n$	[Co(hfac)$_2$ (BPNN)]$_n$	[Co(hfac)$_2$(o-ethoxy phenylNN)]$_n$	[Co(hfac)$_2$(Naph NN)]$_n$
Co-O(1)$_{rad}$	2.03	2.03	2.10	2.04	2.04	2.04	2.03
Co-O(2)$_{rad}$	2.11	2.07	2.11	2.05	2.07	2.04	2.11
O(1)$_{rad}$-Co-O(2)$_{rad}$	81.64	82.85	85.30	80.54	85.44	81.25	82.82

Supplementary Table 3. Hydrogen bonds [Å] and the angles [°] for **1,** [Co(hfac)$_2$(NITPhOMe)]$_n$[4],[Co(hfac)$_2$(PyrNN)]$_n$[5],[Co(hfac)$_2$(BPNN)]$_n$[6], [Co(hfac)$_2$(*o*-ethoxyphenylNN)]$_n$[7] and[Co(hfac)$_2$(NaphNN)]$_n$[8]. The blue highlighted hydrogen bonds are responsible for the intrachain Co-R contact.

C-H···O(N, F)	Compound 1'	Compound 1	[Co(hfac)$_2$ (NITPhOMe)]$_n$	[Co(hfac)$_2$ (PyrNN)]$_n$	[Co(hfac)$_2$ (BPNN)]$_n$	[Co(hfac)$_2$(*o*-ethoxyphenylNN)]$_n$	[Co(hfac)$_2$ (NaphNN)]$_n$
C10···O1(H10···O1)/C10-H10-O1	3.107(2.574)/115.8						
C15···O4(H15B···O4)/C15-H15B-O4	3.186(2.530)/124.3						
C21···F3(H21···F3)/C21-H21-F3	2.751(2.405)/101.1						
C21···F5(H21···F5)/C21-H21-F5	2.725(2.364)/102.0						
C6···O6(H6a···O6)/C6-H6a-O6		3.538(2.591)/162.5					
C11···F7(H11···F7)/C11-H11-F7		3.269(2.526)/135.3					
C16···O2(H16···O2)/C16-H16-O2		2.932(2.449)/111.4					
C16···N2(H16···N2)/C16-H16-N2		3.142(2.553)/120.3					
C20···F4(H20···F7)/C20-H20-F4		2.720(2.358)/102.1					
C16···F5(H16···F5)/C16-H16-F5		3.202(2.803)/106.3					
C7···O7(H7c···O7)/C7-H7c-O7		3.134(2.657)/110.3					
C15···O3(H15···O3)/C15-H15-O3			2.960(2.515)/109.7				
C19···O6(H19B···O6)/C19-H19B-O6			3.020(2.529)/111.8				
C14···F4(H14A···F4)/14-H14A-F4				3.129(2.443)/126.7			
C16···O4(H16B···O4)/C16-H16B-O4				3.265(2.559)/129.0			
C21···N1(H21···N1)/C21-H21-N1				3.205(2.621)/120.1			
C21···O5(H21···O5)/C21-H21-O5				2.963(2.441)/114.4			
C40···O8(H43···O8)/C40-H43-O8						2.980(2.475)/113.2	
C33···O12(H36···O12)/C33-H36-O12						3.179(2.241)/169.0	

C36···O9(H40···O9)/C36-H40-O9	2.985(2.523)/110.0	
C31···O11(H30···O11)/C31-H30-O11	3.443(2.560)/154.5	
C31···O14(H30···O14)/C31-H30-O14	3.134(2.521)/122.3	
C4···O4(H3···O4)/C4-H3-O4		3.117(2.300)/143.6
C5···F7(H4···F7)/C5-H4-F7		3.263(2.544)/132.6
C7···O5(H12···O5)/C7-H12-O5		3.378(2.485)/156.8
C23···F9(H23···F10)/C23-H23-F9		2.689(2.299)/103.8
C18···F3(H22···F3)/C18-H22-F3		2.715(2.392)/99.5
C18···F4(H22···F4)/C18-H22-F4		2.754(2.405)/101.3
C7···F7(H11···F7)/C7-H11-F7		3.467(2.541)/164.9
C7···F11(H10···F11)/C7-H10-F11		3.094(2.442)/125.7
C17···F1B(H4C···F1B)/C17-H4C-F1B		3.455(2.538)/155.6
C17···O1(H4C···O1)/C17-H4C-O1		3.131(2.515)/120.6
C14···O2(H7C···O2)/C14-H7C-O2		3.324(2.570)/133.7
C26···O5(H16···O5)/C26-H16-O5		2.970(2.458)/113.6
C26···N1(H16···N1)/C26-H16-N1		3.193(2.609)/120.0
C8···F9(H20···F9)/C8-H20-F9		2.755(2.411)/101.0
C8···F9(H20···F9)/C8-H20-F9		3.423(2.503)/162.7
C3···F2B(H25···F2B)/C8-H25-F2B		2.629(2.263)/101.9

Supplementary Table 4. The coercive field and squareness for selected SMMs and SCMs.

Compound	H_c (kOe)	Squareness	Ref.
[K(18-crown-6)]{[(Me$_3$Si)$_2$N]$_2$(THF)Dy}$_2$(μ-η^2:η^2-N$_2$)	1.5 (2 K)	93%	[9]
[Co(hfac)$_2$(NITPhOMe)]$_n$	10 (2 K)	46%	[4]
[Co(hfac)$_2$(BPNN)]$_n$	52 (6 K)	86%	[6]
[Co(hfac)$_2$(PyrNN)]$_n$	32 (8 K)	59%	[5]
[Co(hfac)$_2$(NaphNN)]$_n$	30 (8 K)	58%	[8]
{[(Me$_3$Si)$_2$N]$_2$(THF)Tb}$_2$(μ-η^2:η^2-N$_2$)$^-$	50 (11 K)	87%	[10]
[(Cp$^*_2$Dy)$_2$(μ-bpym$^{\bullet}$)](BPh$_4$)	6 (3 K)	80%	[11]
[Co(hfac)$_2$(o-ethoxyphenylNN)]$_n$	54 (6 K)	80%	[7]
Y–diluted [Dy(Cy$_3$PO)$_2$(H$_2$O)$_5$]Br$_3$·2(Cy$_3$PO)·2H$_2$O·2EtOH	14 (2 K)	87%	[12]
[Co(hfac)$_2$(MeNapNOIT)]$_n$	60 (2-7 K)	97%	Compound **1**

Supplementary Table 5. The parameters of the Cole-Cole plots of **1** fitted by the general Debye models in the single-relaxation-process regime.

1-1000 Hz				100-10000 Hz			
T / K	χ_S	χ_T	α	T / K	χ_S	χ_T	α
26	4.30	49.39	0.63	17	6.82E-3	6.50	0.01
28	5.53	48.39	0.61	18	4.66E-3	7.92	0.02
30	6.84	47.69	0.60	19	0	10.11	0.04
32	9.25	46.87	0.57	20	0	12.17	0.07
34	12.49	46.18	0.53	21	0	14.13	0.10
36	15.15	45.77	0.50	32	10.10	56.52	0.57
38	17.40	45.57	0.47	33	10.94	55.98	0.56
40	20.20	45.27	0.46	34	11.82	55.60	0.55
42	24.99	44.67	0.44	35	12.62	55.31	0.54
44	29.66	43.50	0.43	36	13.59	54.96	0.53
46	34.74	41.50	0.43	37	14.90	54.54	0.51
48	34.90	38.25	0.49	38	16.34	54.13	0.50
				39	18.49	53.54	0.47
				40	20.78	52.95	0.44
				41	13.21	51.70	0.41
				42	12.57	51.70	0.39
				43	25.59	50.95	0.39
				44	27.12	19.82	0.37
				45	29.51	48.37	0.35
				46	29.70	46.48	0.34
				47	24.45	44.18	0.37
				48	29.82	41.42	0.35

Supplementary Table 6. Linear combination of two modified Debye model fitting parameters of **1** in the double-relaxation-process regime.

1-1000 Hz	$\Delta\chi_1$	$\Delta\chi_2$	τ_1	τ_2	α_1	α_2	$\chi_{S,tot}$
18 K	48.87	6.50	7.07	7.60E-3	0.46	0.12	0
20 K	42.19	5.89	0.83	1.02E-3	0.55	0.04	0
22 K	41.11	5.57	0.14	2.27E-4	0.58	0	0
24 K	40.28	6.44	0.034	6.00E-5	0.58	0	0
100-10000 Hz	$\Delta\chi_1$	$\Delta\chi_2$	τ_1	τ_2	α_1	α_2	$\chi_{S,tot}$
22 K	68.47	13.08	1.13E-1	2.24E-4	0.32	0.13	0
23 K	51.42	12.57	4.90E-2	1.09E-4	0.42	0.12	0
24 K	46.43	12.32	2.35E-2	5.65E-5	0.48	0.10	0
25 K	43.05	13.56	1.13E-2	3.35E-5	0.45	0.13	0
26 K	42.28	13.02	5.82E-3	1.95E-5	0.48	0.11	0
27 K	40.58	13.54	3.17E-3	1.20E-5	0.48	0.11	0
28 K	38.90	13.06	1.67E-3	8.27E-6	0.48	0.07	0.45
29 K	38.36	12.38	9.55E-4	5.89E-6	0.48	0	1.16
30 K	39.13	13.43	6.55E-4	3.71E-6	0.49	0	0.34
31 K	40.23	12.29	4.39E-4	2.58E-6	0.51	0	1.33

Supplementary Table 7. The fitting parameters for dc magnetization relaxation for **1** at the indicated temperature region.

T / K	11	12	13	14
M_f	0.18	0.09	0.02	0.01
M_0	1.06	1.27	1.44	1.39
β	0.52	0.36	0.26	0.24
τ / s	4214.15	260.70	24.74	5.29

Supplementary Table 8. A comparison of the structural and magnetic parameters of compound **1** and the compounds reported by Ishida[6] and Novak[5].

Compounds	Co-O1(R) Co-O2(R) /Å	O1(R)-Co-O2(R)/º	d_{min}(Co-Co) /Å intrachain	d_{min}(Co-Co) /Å interchain	[a]The angle between the magnetic vector of Co(II) and the direction that is vertical to 2_1 screw axis / º	H_c/kOe	Square ness	Δ_τ/cm^{-1}	τ_0/ s	[b]J / cm^{-1}	Δ_ξ/cm^{-1}
[Co(hfac)$_2$(PyrNN)]$_n$ Ref. 5	2.04/2.05	80.54	7.482	11.151	5.31	32 (8 K)	59% (2 K)	262±13; 275±5	(7±5)×10^{-10} (6±3)×10^{-12}	-161±7	256±9
[Co(hfac)$_2$(BPNN)]$_n$ Ref. 6	2.04/2.07	85.44	7.466 7.430	10.367	2.88 12.58	52 (6 K)	86%	243	6.8 × 10^{-13}		
Compound **1**	2.03/2.07	82.85	7.512	10.487	3.00	60 (2-7 K)	97%	297±7; 254±3	(4.2±0.6)×10^{-10} (1.5±0.6)×10^{-11}	-167±3	269±2

[a]The angles are from *ab initio* calculations. [b]The exchange coupling (J) was obtained by the fitting χT via $\hat{H} = -J \cdot \hat{S}_1 \cdot \hat{S}_2$ by branch chain model.

Supplementary Table 9. Crystal data and structure refinement for **1'** and **1**.

| Compound	1'	1
CCDC number	1484802	1469453
Empirical formula	$C_{46}H_{44}CoF_{12}N_2O_{10}$	$C_{28}H_{23}CoF_{12}N_2O_7$
Formula Weight	1099.78	786.41
Temperature, K	130	130
Radiation type	Mo$K\alpha$	Mo$K\alpha$
Crystal system	Monoclinic	Orthorhombic
Space group	$C2/c$	$P2_12_12_1$
a, Å	11.5222(13)	11.5400(7)
b, Å	18.710(3)	13.9447(7)
c, Å	22.354(3)	19.7558(11)
α, deg	90	90
β, deg	96.78	90
γ, deg	90	90
V, Å^3	4785.4(12)	3179.2(3)
Z	4	4
D_{calcd}, g cm^{-3}	1.527	1.643
μ, mm^{-1}	0.467	0.658
F(000)	2252.0	1584.0
Data / parameter	4214 / 335	5464 / 456
2θ range,deg	6.56 - 50.02	5.84 - 50.02
Reflections collected	8816	12923
Independent reflections	4214	5464
Index ranges	-13 ≤ h ≤ 13 -13 ≤ k ≤ 22 -20 ≤ l ≤ 26	-13 ≤ h ≤ 13 -15 ≤ k ≤ 16 -23 ≤ l ≤ 16
R_{int} / [a]GOF on F^2	0.0781 / 1.053	0.0586 / 1.055
[b]R_1, wR_2 [I>2σ(I)]	0.0760, 0.1432	0.0602, 0.1104
[a]R_1, wR_2(all data)	0.1233, 0.1669	0.0826, 0.1227
Largest diff. peak and hole, e Å^{-3}	0.54 / -0.81	0.53 / -0.45

[a]GOF = $[\Sigma[w(F_o^2 - F_c^2)^2]/(n-p)]^{1/2}$ where n is the number of reflections and p is the total number of parameters refined. [b]$R_1 = \Sigma||F_o| - |F_c|| / \Sigma|F_o|$; $wR_2 = [\Sigma[w(F_o^2 - F_c^2)^2] / \Sigma[w(F_o^2)^2]]^{1/2}$.

Supplementary Table 10. Selected bond distances (Å) and angles (°) for **1'** (A–x+1, y, -z+1/2) and **1**.

1'		1	
Co1-O2$_{rad}$	2.025(8)	Co1-O1$_{rad}$	2.024(5)
Co1-O3	2.112(0)	Co1-O2$_{rad}$	2.072(4)
Co1-O4	2.073(4)	Co1-O4	2.051(5)
Co1-O2A$_{rad}$	2.025(8)	Co1-O5	2.067 (5)
Co1-O3A	2.112(0)	Co1-O6	2.076(5)
Co1-O4A	2.073(4)	Co1-O7	2.060(5)
O2$_{rad}$-Co1-O2A$_{rad}$	81.6(4)	O1$_{rad}$ -Co1-O2$_{rad}$	82.8(5)
O2$_{rad}$ -Co1-O3	92.9(4)	O1$_{rad}$-Co1-O4	97.5(2)
O2$_{rad}$ -Co1-O3A	173.7(7)	O1$_{rad}$-Co1-O5	93.3(4)
O2$_{rad}$ -Co1-O4	93.8(9)	O1$_{rad}$-Co1-O6	173.1(2)
O2$_{rad}$ -Co1-O4A	92.9(4)	O1$_{rad}$-Co1-O7	92.4(2)
O2 A $_{rad}$ -Co1-O3	102.0(9)	O2$_{rad}$-Co1-O4	85.9(6)
O2A$_{rad}$ -Co1-O3A	173.7(7)	O2$_{rad}$-Co1-O5	170.4(2)
O2$_{rad}$-Co1-O4	102.0(9)	O2$_{rad}$-Co1-O6	91.5 (8)
O2A$_{rad}$-Co1-O4A	93.8(9)	O2$_{rad}$-Co1-O7	104.6(1)
O3-Co1-O3A	92.6(3)	O4-Co1-O5	85.8(2)
O3-Co1-O4	81.2(5)	O4-Co1-O6	86.1(2)
O3-Co1-O4A	81.2(5)	O4-Co1-O7	166.4(2)
O3A-Co1-O4	173.7(7)	O5-Co1-O6	92.8(2)
O3A-Co1-O4A	102.0(9)	O5-Co1-O7	84.3(2)
O4-Co1-O4A	81.2(5)	O6-Co1-O7	85.1(2)

7.0 Ab Initio Calculation of the Magnetic Axis on Single Co^{II} Fragment
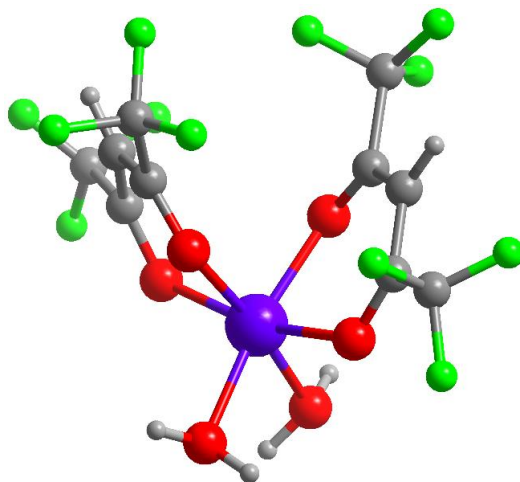

**Supplementary Fig. 20** Model structure of one Co^{II} fragment.

Complete active space second-order perturbation theory (CASPT2) considering the effect of the dynamical electronic correlation based on complete-active-space self-consistent field (CASSCF) using MOLCAS 8.0 program package[13] was performed on the model structure (see Supplementary Fig. 20) extracted from complex **1**.

For the first CASSCF calculation, the basis sets for all atoms are atomic natural orbitals from the MOLCAS ANO-RCC library: ANO-RCC-VTZP for Co^{II} ion; VTZ for close O atoms; VDZ for distant atoms. The calculations employed the second order Douglas-Kroll-Hess Hamiltonian, where scalar relativistic contractions were taken into account in the basis set. The effect of the dynamical electronic correlation was applied using CASPT2 based on the first CASSCF calculation. After that, the spin-orbit coupling was handled separately in the restricted active space state interaction (RASSI-SO) procedure. The active electrons in 10 active spaces considering 3d double shell effect include all seven 3d electrons, and the mixed spin-free states are 50 (all from 10 quadruplets; all from 40 doublets).
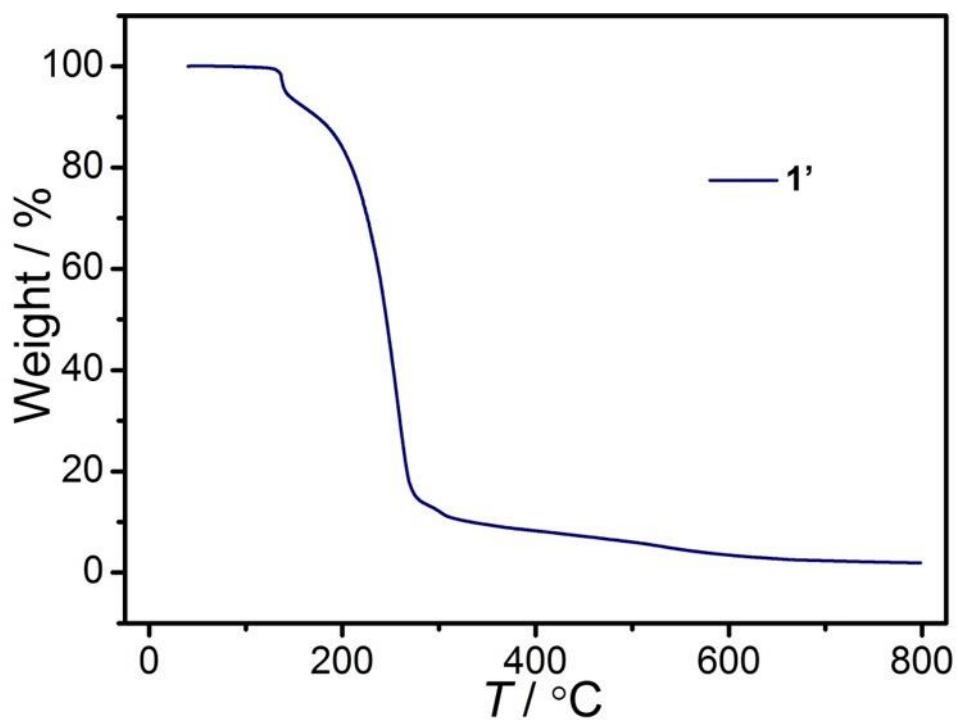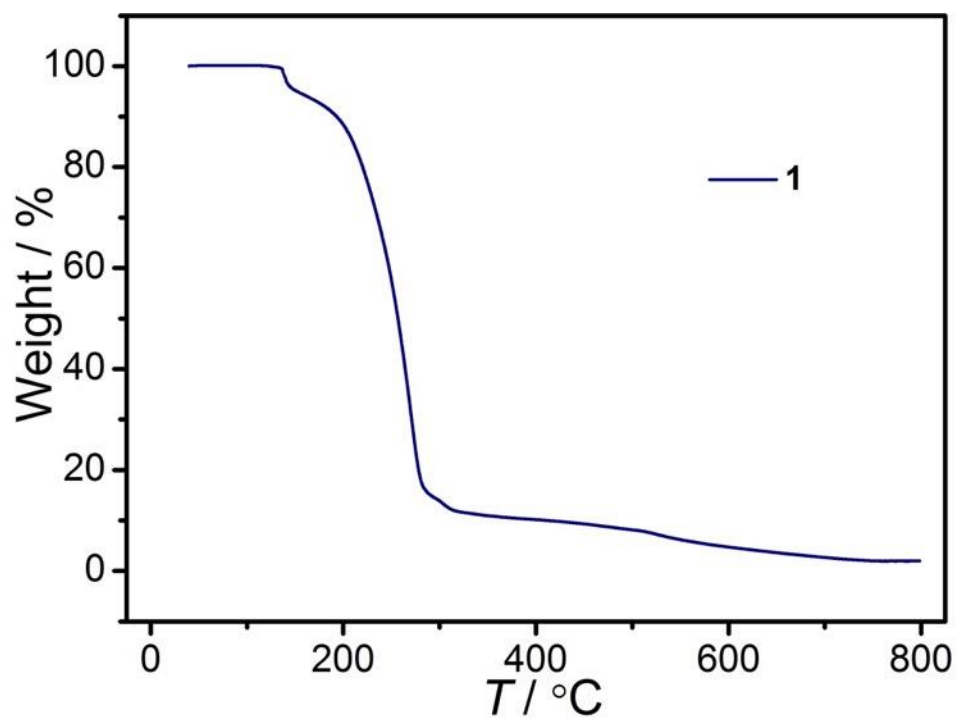
8.0 Other Characterizations
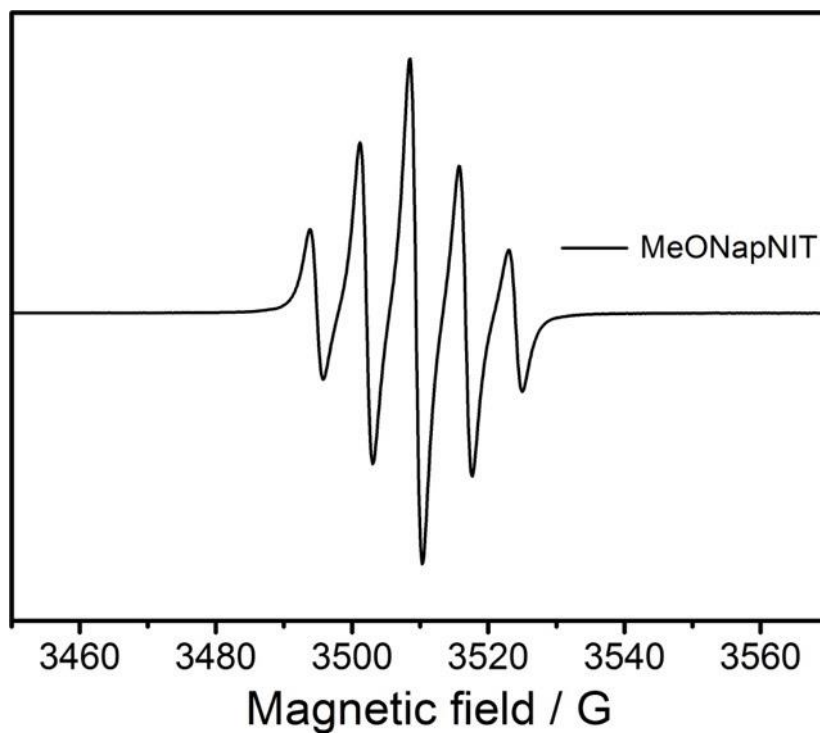
Supplementary Fig. 21 EPR spectrum of the organic radicals MeONapNIT recorded on a Bruker EMX-6/1 spectrometer in benzene at 298 K.
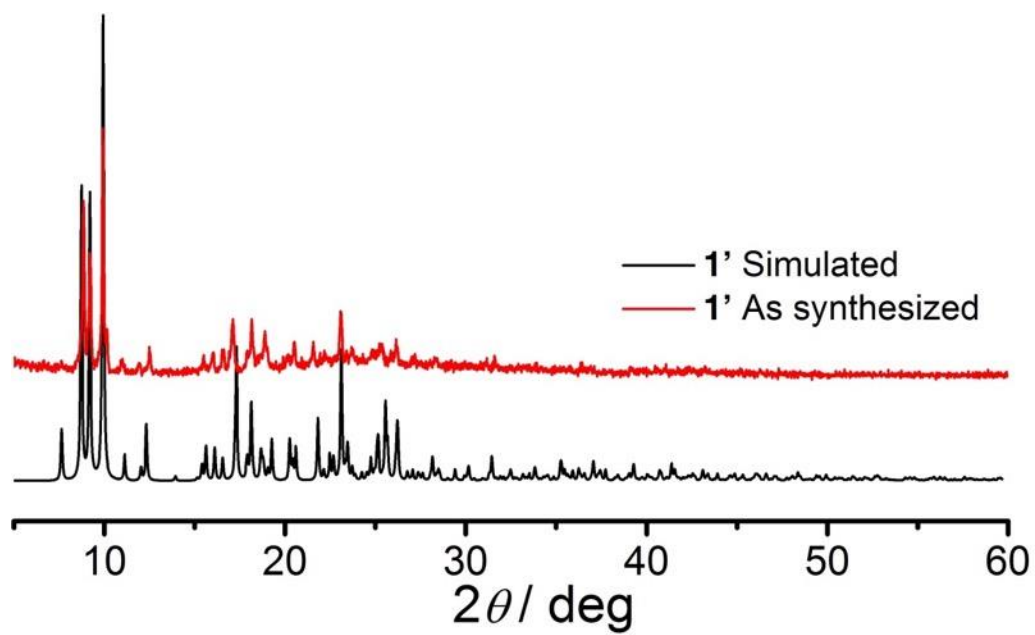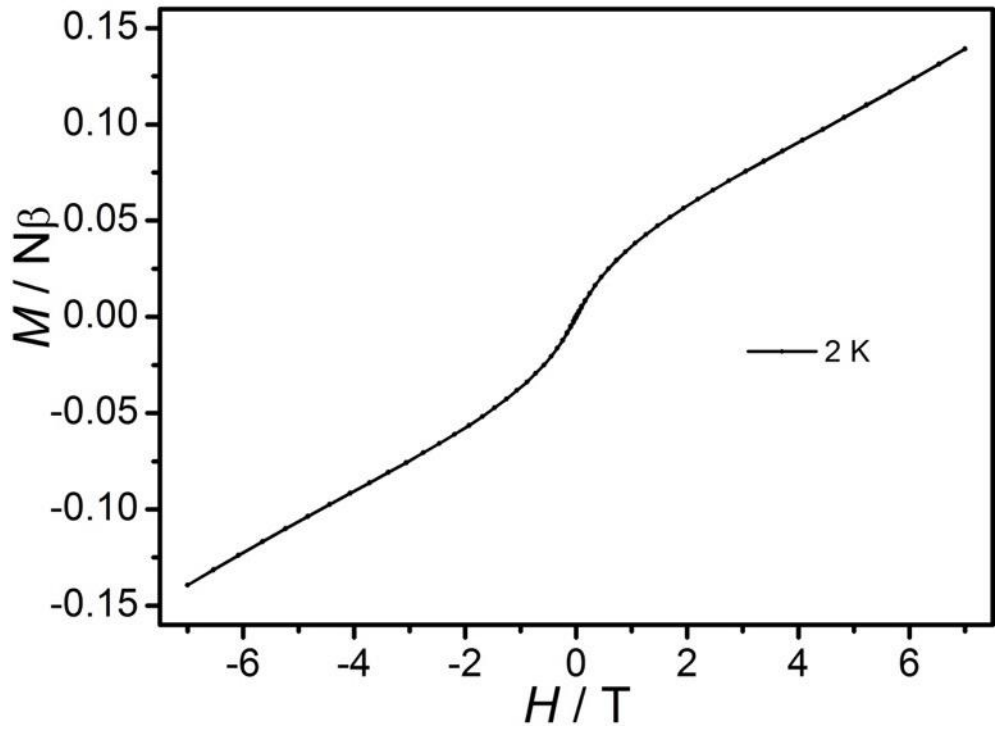
Supplementary Fig. 22 Powder X-ray diffraction of **1'**.

Supplementary Fig. 23 TGA of **1'** in N_2 atmosphere. The sample was heated from room temperature to 800 °C at the heating rate of 10 °C/min.

Supplementary Fig. 24 TGA of **1** in N_2 atmosphere. The sample was heated from room temperature to 800 °C at the heating rate of 10 °C/min.

Supplementary Fig. 25 Hysteresis loop measurement of **1'** at 2 K.

9.0 References

1. Sheldrick, G. M. A short history of SHELX. *Acta Cryst.* **64**, 112–122(2008).

2. Titiš, J & Boča, R. Magnetostructural *D* correlations in hexacoordinated cobalt(II) complexes. *Inorg. Chem.* **50**, 11838–11845 (2011).

3. Ullman, E. F., Osiecki, J. H., Darcy, R. Studies of stable free radicals. X. nitronyl nitroxide monoradicals and biradicals as possible small molecule spin labels. *J. Am. Chem. Soc.* **94**, 7049–7059 (1972).

4. Caneschi, A. *et al.* Cobalt(II)-nitronyl nitroxide chains as molecular magnetic nanowires. *Angew. Chem. Int. Ed.* **40**, 1760–176 (2001).

5. Vaz, M. G. F. *et al.* A cobalt pyrenylnitronylnitroxide single-chain magnet with high coercivity and record blocking temperature. *Chem. Eur. J.* **20**, 5460–5467 (2014).

6. Ishii, N., Okamura, Y., Chiba, S., Nogami, T. & Ishida, T. Giant coercivity in a one-dimensional cobalt-radical coordination magnet. *J. Am. Chem. Soc.* **130**, 24–25 (2008).

7. Okamura, Y., Nogami, T. & Ishida, T. The hardest magnet from a coordination polymer of alternating cobalt(II)-radical heterospins. *Chem. Lett.* **38**, 740–741 (2009).

8. Cassaro, R. A. A. *et al.* A single-chain magnet with a very high blocking temperature and a strong coercive field. *Inorg. Chem.* **54**, 9381−9383 (2015).

9. Rinehart, J. D., Fang, M., Evans, W. J. & Long, J. R. Strong exchange and magnetic blocking in N_2^{3-}-radical-bridged lanthanide complexes. *Nat. Chem.* **3**, 538–542 (2011).

10. Rinehart, J. D., Fang, M., Evans, W. J. & Long, J. R. A N_2^{3-} radical-bridged terbium complex exhibiting magnetic hysteresis at 14 K. *J. Am. Chem. Soc.* **133**, 14236–14239 (2011).

11. Demir, S., Zadrozny, J. M., Nippe, M. & Long J. R. Exchange coupling and magnetic blocking in bipyrimidyl radical-bridged dilanthanide complexes. *J. Am. Chem. Soc.* **134**, 18546–18549 (2012).

12. Chen Y-C. *et al.* Symmetry-supported magnetic blocking at 20 K in pentagonal

bipyramidal Dy(III) single-ion magnets. *J. Am. Chem. Soc.* **138**, 2829–2837 (2016).

13. Karlstrom, G. *et al.* MOLCAS: a program package for computational chemistry. *Comput. Mater. Sci.* **28**, 222–239 (2003).